TIME-DEPENDENT ADJOINT-BASED OPTIMIZATION OF PHOTONIC CRYSTALS AND METAMATERIALS USING A STABILIZED FINITE ELEMENT FORMULATION

By

Xueying Zhang

James C. Newman III
Professor of Mechanical Engineering
(Chair)

W. Kyle Anderson
Professor (Retired)
(Committee Member)

Kidambi Sreenivas
Research Professor of
Mechanical Engineering
(Committee Member)

Abdollah Arabshahi
Research Professor of
Mechanical Engineering
(Committee Member)

TIME-DEPENDENT ADJOINT-BASED OPTIMIZATION OF PHOTONIC CRYSTALS AND METAMATERIALS USING A STABILIZED FINITE ELEMENT FORMULATION

By

Xueying Zhang

A Dissertation Submitted to the Faculty of the University
of Tennessee at Chattanooga in Partial Fulfillment
of the Requirements of the Degree of Doctor of Philosophy
in Computational Engineering

The University of Tennessee at Chattanooga
Chattanooga, Tennessee

May 2017

ABSTRACT

In the current research, a time-dependent discrete adjoint algorithm for optimization of electromagnetic problems is developed. The proposed algorithm improves the efficiency for gradient-based optimization. The time-dependent Maxwell equations are discretized using a semi-discrete Petrov-Galerkin method, and time advancement is accomplished with an implicit, second-order backward differentiation formulation (BDF2). Utilizing the developed capability, two gradient-based shape design optimizations are conducted. In the first optimization an optical waveguide is designed with photonic crystals, and in the second an all-dielectric metamaterial is designed.

A motivation for optimizing photonic crystals is due to their use as multi-band optical waveguides for telecommunication applications. For this design optimization, to ensure smooth surfaces, Bezier curves are employed to parametrically represent the shape. To reflect the design changes on the mesh, linear elasticity is used to adapt interior mesh points to boundary modifications. The cost function used in this design attempts to shift the band gap of the photonic crystals to desired frequency ranges. Results demonstrate a band gap shift from one single band gap to multiple band gaps is achievable.

The motivation for optimizing broadband metamaterials is for their use as dielectric mirrors for applications where high power reflection is required. In this optimization, Hicks-Henne functions are utilized for shape parameterization and linear elasticity used once again for mesh adaptation. The cost function used attempts to widen

the bandwidth of the metamaterial over a desired frequency range. Results demonstrate an increase of the full width at half maximum (FWHM) of reflection from 111THz to 303THz.

ACKNOWLEDGEMENTS

First of all, I would like to thank Dr. James C. Newman and Dr. W. Kyle Anderson for their countless hours of advising, reading, encouraging, and patience throughout the entire process. I also thank Dr. Kidambi Sreenivas and Dr. Abdollah Arabshahi for serving on my committee. Finally, I would like to acknowledge and thank SimCenter for providing me academic training and support to the research for the dissertation.

TABLE OF CONTENTS

ABSTRACT iii

ACKNOWLEDGEMENTS v

LIST OF TABLES viii

LIST OF FIGURES ix

CHAPTER

I. INTRODUCTION 1

Photonic Crystals 1
Metamaterial 2
Numerical Methods in Computational Electromagnetics 5
Petrov-Galerkin Methods for Time-Domain Simulations and Adjoint based Formulation for Shape Optimization 6

II. PETROV-GALERKIN METHODS FOR ELECTROMAGNETIC SIMULATIONS AND TIME-DEPENDENT SHAPE SENSITIVY ANALYSIS 8

Petrov-Galerkin Methods for Electromagnetic Simulations 8
Governing Equations 8
Finite Element Formulation 10
Shape Functions for FEM 12
Boundary Conditions 14
Time-dependent Shape Sensitivity Analysis 16
Sensitivity Analysis 17
Finite Difference Method 17
Forward Mode Direct Differentiation 17
Reverse Mode Discrete Adjoint Formulation 19
Surface Parameterization 20
Linear-Elastic Smoothing 20
Hicks-Henne Function 22
Bezier Curve 23

III. PHOTONIC CRYSTALS: THEORY, SIMULATION AND RESULTS 24

Introduction 24

Calculation of Band Diagram 25
Floquet-Bloch Periodic Conditions 25
Square Lattice 25
Triangular Lattice 26
Reciprocal Lattice and Brillouin Zone 28
Square Lattice 29
Triangular Lattice 32
Excitation and Monitoring 35
Simulation Results of Photonic Band Gaps 36
Square Lattice 36
Triangular Lattice 38
Approach Array Model 41
Reflection and Transmission 41
Square Lattice 42

IV. SENSITIVITY ANALYSIS AND SHAPE OPTIMIZATION OF PHOTONIC CRYSTALS 44

Cost Function and Sensitivity Analysis 44
Forward Sensitivity 45
Discrete Adjoint Formulation 47
Verification of Shape Sensitivity Derivatives 49
Optimization Results and Application on Optical waveguide 50
Photonic Crystal Waveguide 50
Design of Dual-band Waveguide 52
Design of Triple-band Waveguide 54

V. SIMULATION AND OPTIMIZATION OF METAMATERIAL 57

All-dielectric Metamaterial and Optimization 57
Proposed Design Model 57
Results and Accuracy 58
Optimization of All-dielectric Metamaterial 58
Simulation of 3D Metamaterial Model 61

VI. CONCLUSION 64

REFERENCES 66

VITA 71

LIST OF TABLES

Table 3.1 Wave Vectors in the Irreducible Brillouin Zone of Square Lattice 31

Table 3.2 Wave Vectors in the Irreducible Brillouin Zone of Triangular Lattice 34

Table 4.1 Comparison of Sensitivity Derivatives 49

LIST OF FIGURES

Figure 2.1 Nodes of triangular element 12

Figure 2.2 Nodes of tetrahedron element.....13

Figure 3.1 Square lattice structure and unit cell 26

Figure 3.2 Triangular lattice structure and unit cell.....27

Figure 3.3 The real and reciprocal lattice of the square lattice.....30

Figure 3.4 The Brillouin zone and irreducible Brillouin zone of the square lattice.....31

Figure 3.5 The real and reciprocal lattice of the triangular lattice.....33

Figure 3.6 The Brillouin zone and irreducible Brillouin zone of the triangular lattice 34

Figure 3.7 Frequency spectra at each wave vector for square lattice 37

Figure 3.8 Band diagram of square lattice.....38

Figure 3.9 Frequency spectra at each wave vector for triangular lattice 39

Figure 3.10 Band diagram of triangular lattice.....40

Figure 3.11 Approach array model for square lattice 42

Figure 3.12 Results of approach array model for square lattice 43

Figure 4.1 Comparison of sensitivity at each frequency for square lattice.....50

Figure 4.2 Electric field pattern in photonic crystal waveguide for frequency f=500THz.....51

Figure 4.3 Shape of optimized unit cell for dual-band optical waveguide 53

Figure 4.4 Band diagram of optimized photonic crystals for dual-band

waveguide 53

Figure 4.5 Electric field pattern in designed dual-band waveguide.....54

Figure 4.6 Shape of optimized unit cell for triple-band waveguide 55

Figure 4.7 Band diagram of optimized photonic crystal for triple-band waveguide 56

Figure 4.8 Electric field pattern in designed triple-band waveguide 56

Figure 5.1 Proposed initial metamaterial model 57

Figure 5.2 Simulation results of initial model 58

Figure 5.3 Comparison of reflection over 300-700THz 59

Figure 5.4 Electric field distribution at 426THz 60

Figure 5.5 Electric field distribution of model with nine design variables.....60

Figure 5.6 SEM images of periodic Si cylinder-based metamaterials[44] 62

Figure 5.7 Simulation Results of Reflectance of 3D Metamaterial 63

CHAPTER I

INTRODUCTION

Photonic Crystals

Over the last century, advances in semiconductor physics have significantly changed our daily lives. The semiconductor technology utilizes the electrical properties of certain materials and initiates the transistor revolution in electronics. However, traditional semiconductor materials have limitation in realizing the goal of miniaturization and high-speed performance of integrated electronic circuits. Miniaturization leads to increased resistance and higher power dissipation, while higher speeds cause greater sensitivity in signal synchronization. To overcome these problems, photonic integrated circuits, which use light instead of electrons as information carrier, have been proposed as alternative technologies. As the information carrier, light has several advantages over the electron[1]. First, the speed of light in a dielectric material is much higher than that of an electron in a metallic wire. Next, the amount of information that light can carry per second is much larger. In addition, the bandwidth of optical communication systems is typically on the order of one terahertz, and is much larger compared with that of electronic systems, which is on the order of one hundred kilohertz. Moreover, photons interact less than electrons and result in reduction of energy losses.

To control the optical properties of materials, in the late 1980s, a new class of optical materials, known as photonic crystals, was proposed[2]. The photonic crystal is

the optical analogue of real electronic semiconductor crystal. Photonic crystals consist of macroscopic dielectric media in a periodic arrangement, while electronic semiconductor crystals have a periodic arrangement of atoms. In electronic semiconductor crystals, there are gaps in the energy band structure, where electrons with certain electron energies are forbidden to propagate. Similarly, photonic crystals have gaps where light with certain photon energies are forbidden to propagate, and these gaps are named the photonic band gaps. More details of the photonic band gap will be discussed in Chapter III.

With the development of photonic crystals, light can be controlled to propagate only in certain directions, or be confined within a specified volume. Therefore, the photonic crystal related devices have been applied in the fields of telecommunication, sensing, high-speed computing, spectroscopy, etc. In this dissertation, the photonic band gap of 2D photonic crystal is simulated using the Petrov-Galerkin finite element method. The optimization of the photonic band gap is carried out using a gradient-based approach with the adjoint formulation being employed for sensitivity calculation. Using this optimization method, we designed an optical waveguide based on photonic crystal with multiple bands, which can potentially be used for applications such as optical communication.

Metamaterial

Metamaterial is defined as an artificially structured and effectively homogenous material with properties that arise from the structuring of the material rather than the constituent materials. The properties of metamaterial correspond to time varying fields such as electromagnetic field and acoustic field. The research in this dissertation focuses on the electromagnetic metamaterials. The optical properties of metamaterials depend on

the constituent materials and geometries of the building blocks. Compared to photonic crystal, one significant difference of metamaterial is that the building blocks of metamaterials are much smaller than wavelength. As a result, light passing through a metamaterial does not diffract and therefore material can exhibit 'effective' material properties, for example, refractive index, permittivity and permeability, different from the naturally existing materials. Therefore, one can design such metamaterials to realize unique material properties not attainable with naturally occurring materials, opening up the pathway for many applications.

In 1999, Pendry[3] designed a material with a negative index of refraction. In 2000, Smith[4] first experimentally realized a negative index medium using periodic arrays of SRRs and a cut-wires. Since then, different types of metamaterials have been developed with characteristics of near-zero permittivity[5, 6], chirality[7, 8], super absorption[9], negative group velocity[10, 11], and highly anisotropic material properties[12, 13]. In 2005, Pendry[14] proposed a new application for metamaterial: the electromagnetic cloaking device. The electromagnetic cloak was first realized at microwave frequencies[12] in 2006 and has been demonstrated at optical frequencies[15] in 2009. The electromagnetic cloak is widely applied as source transformations[16], electromagnetic black holes[17, 18], novel lenses[19], and hybrid optical devices [20]. In recent years, metamaterials have also been demonstrated in applications such as thermal sensing, solar energy harvesting and optoelectronics applications [21-27].

Since metal-based metamaterials have limitations such as absorption caused by ohmic damping[28-30] and saturation of the magnetic response at high frequencies[31], all-dielectric metamaterials have been proposed as an alternative approach. Dielectric materials do not cause magnetic saturation at high frequencies. Dielectric materials result

in less optical absorption than metal does at high frequencies. All-dielectric metamaterials have been developed to realize high frequency magnetism[32-36] and negative refractive index[37, 38]. Recently, dielectric metamaterials have been developed that control the phase of reflected light[39], achieve negative phase propagation[40], active tuning of resonant modes[41], and for the demonstration of magnetic mirror with zero reflection phase[42].

In particular, dielectric metamaterial mirrors have been an emerging research topic due to their ability to control light reflection with desired patterns[43-45]. If designed correctly, the dielectric metamaterial mirrors can be designed to perfectly reflect light at desired wavelength, with reflection exceeding the traditional metal mirror. Moreover, due to the low loss nature and high stability of the constituent dielectric materials, dielectric metamaterial mirror is particularly beneficial in applications where high power light reflection is required. On the other hand, comparing with the multilayer film stack 1D photonic crystal Bragg mirror, one can achieve perfect light reflection with a much smaller thickness, therefore opening up pathways for applications such as integrated photonics and optical communications. However, previous metamaterial mirror work mainly focused on simple geometry shapes such as cylinders. Optimization of the geometry of dielectric metamaterials with complex shapes has not been extensively explored. It is shown in Chapter V of this dissertation that by employing shape optimization method, further improvements in the performance of the dielectric metamaterial mirror can be achieved.

Numerical Methods in Computational Electromagnetics

A variety of numerical methods are used in solving electromagnetic problems, such as the finite-difference time-domain method, the finite-volume method and the finite-element method.

In the 1960's, Yee[46] invented the finite-difference time-domain method (FDTD) that solved Maxwell's equations discretized on structured grids directly in the time domain. The method is efficient since no matrix solutions need to be calculated and also has ease of implementation and simple grid generation requirements. However, FDTD suffers from the limitation in its capability to model complex geometrical structures such as curved surfaces and devices with a widely varying range of geometric scales. FDTD is widely applied in computational electromagnetics, for instance, the CST Microwave Studio [47] is a Finite Integral Technique (FIT) solver, which is basically FDTD with integration instead of differentiation. CST MICROWAVE STUDIO®(CST MWS) is a specialist tool for the 3D EM simulation of high frequency components.

The finite-volume method is another approach applied in computational electromagnetics. Maxwell's equations in this form have mathematical similarities with the compressible Euler equations from fluid dynamics. These relationships are taken advantage of by the finite-volume method in solving the Maxwell's equations [48, 49]. However, the second-order accuracy resulting from discretization of the spatial derivatives in this method is not sufficient to solve problems requiring higher-order accuracy such as those found in high-frequency applications and electrically large structures.

The finite-element method was introduced to computational electromagnetics by Jin in his book [50]. Although not as widely used as FDTD, it has many advantages such as the capability for modeling both complex structures and materials. The method can accurately model curved surfaces and complex structures by applying unstructured meshes with curvilinear triangular and tetrahedral elements. Although the method requires solving a large matrix equation, solution can be obtained efficiently using advanced solvers. The commercial simulation software HFSS [51] is based on the finite element method. The High Frequency Structure Simulator (HFSS™) is a software tool for 3D full-wave electromagnetic field simulations. The metamaterial model discussed in this dissertation is simulated with HFSS for comparison.

Petrov-Galerkin Methods for Time-Domain Simulations and Adjoint based Formulation for Shape Optimization

Maxwell's equation can be cast in both the time domain and the frequency domain, and consequently the numerical simulation can be applied in either the time domain or the frequency domain. The frequency-domain numerical method is highly suitable for scattering analysis, where the main concern is the scattering due to plane waves from many incident directions. The time-domain numerical method is well suited for the current work where solutions over a broad frequency band are desired. The broadband frequency-domain solution can be obtained through the Fourier transform in one time-domain calculation.

Petrov-Galerkin finite element methods are applied to solve Maxwell's equations for applications involving photonic crystals and metamaterials in this work. The method is highly suitable for analysis and design of periodic electromagnetic structures. It has the

capability of dealing with high-order spatial discretization, which helps represent complex geometries accurately. The Petrov-Galerkin method has been successfully applied in computational fluid dynamics [52] and computation electromagnetics[53, 54].

The automatic computational shape optimization is a novel alternative for designing optical structures such as photonic crystals and metamaterials. Discrete Adjoint formulation in gradient-based optimization realizes efficiency in calculation of the sensitivity of cost function with multiple design variables, since the computational costs do not scale with the number of design variables. Adjoint-based shape optimization has been applied using finite-volume methods in a steady flow environment in the area of aerodynamics[55-58]. In 2000, Li[59] developed an unsteady discrete adjoint algorithm for high-order discontinuous Galerkin discretizations in time-dependent flow problems and applied this technique to unsteady shape optimization problems. Recently, Lin[60-63] applied shape and topology optimization for the design of acoustic metamaterial with a discrete adjoint formulation. Applications included noise reduction, design of effective material property, and an acoustic cloaking device. In this work, the discrete adjoint formulation is applied to Petrov-Galerkin discretizations of Maxwell's equations for shape optimization of photonic crystals and electromagnetic metamaterials. The technique is applied to design a multiband optical waveguide and a broadband perfect reflector mirror[64].

CHAPTER II

PETROV-GALERKIN METHODS FOR ELECTROMAGNETIC SIMULATIONS AND TIME-DEPENDENT SHAPE SENSITIVY ANALYSIS

Petrov-Galerkin Methods for Electromagnetic Simulations

Governing Equations

Maxwell's equations are the basic laws in electromagnetics that describe electric and magnetic phenomena. The time dependent Maxwell's equation set is given by:

$$\nabla\times\boldsymbol{E} = -\frac{\partial \boldsymbol{B}}{\partial t} - \boldsymbol{M} \tag{2.1}$$

$$\nabla\times\boldsymbol{H} = \frac{\partial D}{\partial t} + \boldsymbol{J} \tag{2.2}$$

$$\nabla \cdot \boldsymbol{B} = 0 \tag{2.3}$$

$$\nabla \cdot \boldsymbol{D} = \rho_c \tag{2.4}$$

where $\boldsymbol{E}$ is the electric field, $\boldsymbol{H}$ is the magnetic field, $\boldsymbol{D}$ is the electric flux density and $\boldsymbol{B}$ is the magnetic flux density. The magnetic current density $\boldsymbol{M}$, the electric current density $\boldsymbol{J}$ and the electric charge density ρ_c are all ignored in the various applications considered in the current work.

The flux densities and the field intensities have the following relationships:

$$B = \mu H \tag{2.5}$$

$$D = \varepsilon E \tag{2.6}$$

where μ is the permeability and ε is the permittivity.

For three-dimensional applications, the governing equations are rewritten in a divergence form as follows:

$$\frac{\partial \boldsymbol{q}}{\partial t} + \nabla \cdot \boldsymbol{F}(\boldsymbol{q}) = 0 \tag{2.7}$$

$$\boldsymbol{q} = (D_x, D_y, D_z, B_x, B_y, B_z)^T \tag{2.8}$$

$$\boldsymbol{F} = \hat{\imath}\boldsymbol{f} + \hat{\jmath}\boldsymbol{g} + \hat{k}\boldsymbol{h} \tag{2.9}$$

$$\boldsymbol{f} = (0, H_z, -H_y, 0, -E_z, E_y)^T \tag{2.10}$$

$$\boldsymbol{g} = (-H_z, 0, H_x, E_z, 0, -E_x)^T \tag{2.11}$$

$$\boldsymbol{h} = \left(H_y, -H_x, 0, -E_y, E_x, 0\right)^T \tag{2.12}$$

The equations above can be written in the differential form as:

$$\frac{\partial}{\partial t}\begin{bmatrix} D_x \\ D_y \\ D_z \\ B_x \\ B_y \\ B_z \end{bmatrix} + \frac{\partial}{\partial x}\begin{bmatrix} 0 \\ B_z/\mu \\ -B_y/\mu \\ 0 \\ -D_z/\varepsilon \\ D_y/\varepsilon \end{bmatrix} + \frac{\partial}{\partial y}\begin{bmatrix} -B_z/\mu \\ 0 \\ B_x/\mu \\ D_z/\varepsilon \\ 0 \\ -D_x/\varepsilon \end{bmatrix} + \frac{\partial}{\partial z}\begin{bmatrix} B_y/\mu \\ -B_x/\mu \\ 0 \\ -D_y/\varepsilon \\ D_x/\varepsilon \\ 0 \end{bmatrix} = 0 \tag{2.13}$$

For two-dimensional applications, the fourth term in Eq.(2.13) is not considered, that is $\boldsymbol{h} = \boldsymbol{0}$. For a transverse-electric (TE) mode application, the first, second and sixth rows of Eq.(2.13) are solved, which can be expressed as:

$$\boldsymbol{q} = \left\{D_x, D_y, B_z\right\}^T \tag{2.14}$$

$$\boldsymbol{f} = \left\{0, B_z/\mu, D_y/\varepsilon\right\}^T \tag{2.15}$$

$$\boldsymbol{g} = \{-B_z/\mu, 0, -D_x/\varepsilon\}^T \tag{2.16}$$

For a transverse-magnetic(TM) mode application, the third, fourth and fifth rows of Eq.(2.13) are solved, which can be expressed as:

$$\boldsymbol{q} = \left\{B_x, B_y, D_z\right\}^T \tag{2.17}$$

$$\boldsymbol{f} = \{0, -D_z/\varepsilon, -B_y/\mu\}^T \tag{2.18}$$

$$\boldsymbol{g} = \{D_z/\varepsilon, 0, B_x/\mu\}^T \tag{2.19}$$

Finite Element Formulation

In the Petrov-Galerkin finite-element approach, field variables are assumed continuous across element boundaries. As a result, data is stored at the vertices of the elements. Within each element, the solution is assumed to vary according to a linear combination of polynomial basis functions given by:

$$\boldsymbol{Q}_h = \sum_{i=1}^{n} N_i \boldsymbol{Q}_i \tag{2.20}$$

In Eq.(2.20), $\boldsymbol{Q}_h$ represents the approximated variables within each element dependent on $\boldsymbol{Q}_i$ and N_i, $\boldsymbol{Q}_i$ is the corresponding data at each node of the element, and each N_i represents a basis function.

The Petrov-Galerkin method is formulated as a weighted residual method, which can be expressed in the following form:

$$\oiiint_{\Omega} [\phi] \left(\frac{\partial \boldsymbol{Q}}{\partial t} + \nabla \cdot \boldsymbol{F} \right) \partial\Omega = 0 \tag{2.21}$$

where ϕ is a weighting function defined by the Streamline Upwind/Petrov-Galerkn(SUPG) method given by:

$$[\phi] = N[I] + \left(\frac{\partial N}{\partial x}[A] + \frac{\partial N}{\partial y}[B] + \frac{\partial N}{\partial z}[C] \right)[\tau] = N[I] + [P] \tag{2.22}$$

In Eq.(2.22), the first term $N[I]$ is composed of linear combination of the same basis functions used in Eq.(2.20), and can be represented as:

$$N = \sum_{i=1}^{n} N_i c_i \tag{2.23}$$

where c_i is arbitrary, and n is the number of degrees of freedom in the element. The second term $[P]$, is a stabilizing term that dissipates odd-even point decoupling along preferential directions. In the second term, $[A], [B]$ and $[C]$ are given by:

$$[A] = \left[\partial \boldsymbol{f}/_{\partial \boldsymbol{q}}\right], [B] = \left[\partial \boldsymbol{g}/_{\partial \boldsymbol{q}}\right], [C] = \left[\partial \boldsymbol{h}/_{\partial \boldsymbol{q}}\right] \tag{2.24}$$

And $[\tau]$ represents the stabilization matrix and can be obtained by the following definitions [65]

$$[\tau]^{-1} = \sum_{k=1}^{n} \left|\frac{\partial N_k}{\partial x}[A] + \frac{\partial N_k}{\partial y}[B] + \frac{\partial N_k}{\partial z}[C]\right| \tag{2.25}$$

$$\left|\frac{\partial N_k}{\partial x}[A] + \frac{\partial N_k}{\partial y}[B] + \frac{\partial N_k}{\partial z}[C]\right| = [T][|\Lambda|]\,[T]^{-1} \tag{2.26}$$

where $[T]$ and $[\Lambda]$ are the right eigenvectors and eigenvalues of the matrix on the left side of Eq. (2.26) respectively, and $[T]^{-1}$ represents the inverse of $[T]$. By applying Green's theorem, the weak statement can be expressed as:

$$\iiint_{\Omega}\left(N\left\{\frac{\partial \boldsymbol{q}}{\partial t}\right\} - \boldsymbol{F}\cdot\nabla N\right)\partial\Omega + \iiint_{\Omega}[P]\left(\frac{\partial \boldsymbol{q}}{\partial t} + \nabla\cdot\boldsymbol{F}\right)\partial\Omega + \oiint_{\Gamma} N\boldsymbol{F}\cdot\hat{n}\partial\Gamma = 0 \tag{2.27}$$

Note that the surface integral needs to be evaluated only on the boundaries where appropriate boundary conditions are weakly enforced by incorporating them into the surface integral. Because the field variables are assumed to vary continuously in the interior of the domain, the surface integral typically vanishes on the boundaries of the interior elements. The boundaries mentioned above include not only the physical boundaries of the domain, but also the boundaries of discontinuous materials. The details will be discussed later.

Shape Functions for FEM

In the Petrov-Galerkin scheme, the domain of interest is discretized into a series of non-overlapping elements. For two-dimensional and three-dimensional applications in the current work, the triangular and tetrahedral elements are applied, respectively. The triangular and tetrahedral elements within the computational mesh are mapped to parent elements in non-dimensional (ξ_1, ξ_2) space and (ξ_1, ξ_2, ξ_3) space, respectively.

For a linear triangle with 3 nodes, as shown in Fig. 2.1(a), the shape functions are given by:

$$N(\xi_1, \xi_2) = \begin{bmatrix} N_1 \\ N_2 \\ N_3 \end{bmatrix} = \begin{bmatrix} 1 - \xi_1 - \xi_2 \\ \xi_1 \\ \xi_2 \end{bmatrix} \tag{2.28}$$

For a quadratic triangle with 6 nodes, as shown in Fig. 2.1(b), the shape functions are given by:

$$N(\xi_1, \xi_2) = \begin{bmatrix} N_1 \\ N_2 \\ N_3 \\ N_4 \\ N_5 \\ N_6 \end{bmatrix} = \begin{bmatrix} (1 - \xi_1 - \xi_2)(1 - 2\xi_1 - 2\xi_2) \\ \xi_1(2\xi_1 - 1) \\ \xi_2(2\xi_2 - 1) \\ 4\xi_1(1 - \xi_1 - \xi_2) \\ 4\xi_1\xi_2 \\ 4\xi_2(1 - \xi_1 - \xi_2) \end{bmatrix} \tag{2.29}$$

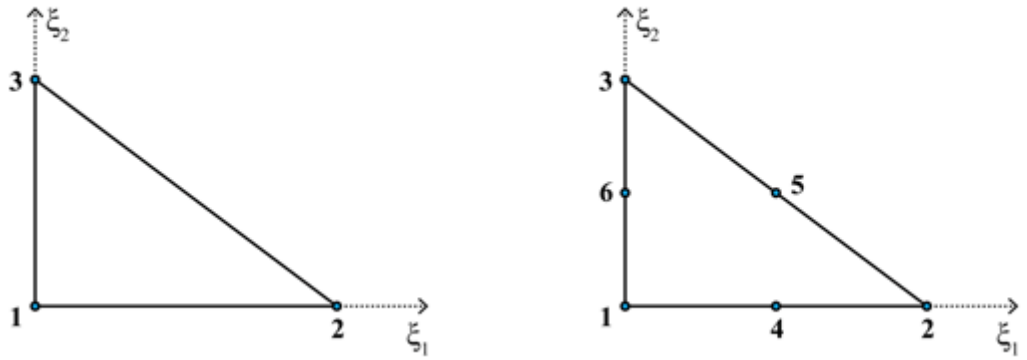

(a) Linear triangular (b) Quadratic triangular

Figure 2.1 Nodes of triangular element

For a linear tetrahedron with 4 nodes, as shown in Fig. 2.2(a), the shape functions are given by:

$$N(\xi_1, \xi_2, \xi_3) = \begin{bmatrix} N_1 \\ N_2 \\ N_3 \\ N_4 \end{bmatrix} = \begin{bmatrix} 1 - \xi_1 - \xi_2 - \xi_3 \\ \xi_1 \\ \xi_2 \\ \xi_3 \end{bmatrix} \tag{2.30}$$

For a quadratic tetrahedron with 10 nodes, as shown in Fig.2.2(b), the shape functions are given by:

$$N(\xi_1, \xi_2, \xi_3) = \begin{bmatrix} N_1 \\ N_2 \\ N_3 \\ N_4 \\ N_5 \\ N_6 \\ N_7 \\ N_8 \\ N_9 \\ N_{10} \end{bmatrix} = \begin{bmatrix} 1 - \xi_1 - \xi_2 - \xi_3 - 0.5(N_5 + N_7 + N_8) \\ \xi_1 - 0.5(N_5 + N_6 + N_9) \\ \xi_2 - 0.5(N_6 + N_7 + N_{10}) \\ \xi_3 - 0.5(N_8 + N_9 + N_{10}) \\ 4\xi_1(1 - \xi_1 - \xi_2 - \xi_3) \\ 4\xi_1\xi_2 \\ 4\xi_2(1 - \xi_1 - \xi_2 - \xi_3) \\ 4\xi_3(1 - \xi_1 - \xi_2 - \xi_3) \\ 4\xi_1\xi_3 \\ 4\xi_2\xi_3 \end{bmatrix} \tag{2.31}$$

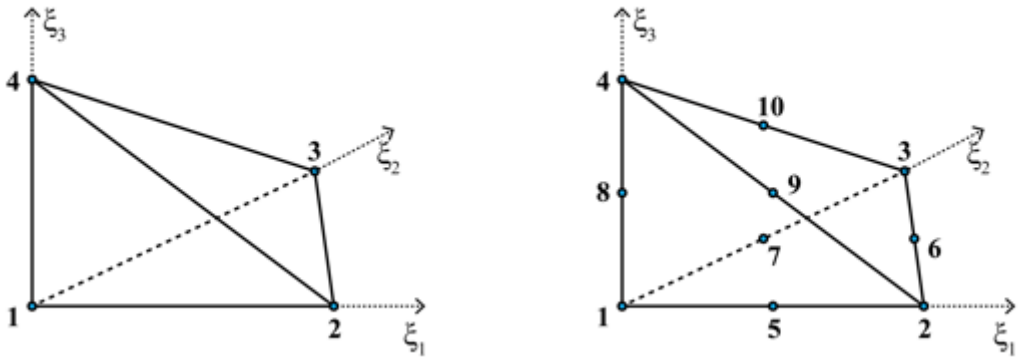

(a) Linear tetrahedron (b) Quadratic tetrahedron

Figure 2.2 Nodes of tetrahedron element

The shape functions discussed above form the basis functions in Eq.(2.20). Gaussian quadrature rules are used in evaluating the volume and surface integrals. In

evaluating the volume integrals, a function integrated over a tetrahedron can be expressed as:

$$\oiiint_{\Omega} f(x,y,z)\partial\Omega = \sum_{i=1}^{N_{gauss}} f_i(x(\xi_1,\xi_2,\xi_3)\,, y(\xi_1,\xi_2,\xi_3)\,, z(\xi_1,\xi_2,\xi_3)\,)W_i J \quad (2.31)$$

where (ξ_1,ξ_2,ξ_3) are Gauss points, W_i are Gauss weights, and J is the Jacobian. In evaluating the surface integrals, a function integrated over a triangle can be expressed as:

$$\iint_{\Gamma} f(x,y)\partial\Gamma = \sum_{i=1}^{N_{gauss}} f_i(x(\xi_1,\xi_2), y(\xi_1,\xi_2))W_i J \quad (2.32)$$

where (ξ_1,ξ_2) are Gauss points, W_i are Gauss weights, and J is the Jacobian.

For polynomial representations of the dependent variables of p, formulas for integrating polynomials of order 2p are used in evaluating volume integrals while formulas for integrating polynomials of order 2p+1 are used in evaluating surface integrals [66].

Boundary Conditions

The boundary conditions are weakly enforced through the flux terms in the surface integral in Eq. (2.27). For applications in the current work, three types of boundary conditions are implemented: Silver-Muller boundary conditions, material jump conditions and Floquet-Bloch periodic conditions.

For Silver-Muller boundary conditions, the flux can be derived from the following equation [67]:

$$(\boldsymbol{E} - c\boldsymbol{B}\times\boldsymbol{n})\times\boldsymbol{n} = e^*\times\boldsymbol{n} \quad (2.33)$$

or, in a similar way,

$$(c\boldsymbol{B} + \boldsymbol{E}\times\boldsymbol{n})\times\boldsymbol{n} = cb^*\times\boldsymbol{n} \quad (2.34)$$

where ($\boldsymbol{E}$,$\boldsymbol{B}$) denotes the electromagnetic field, c is the speed of light and **n** is the unit outside normal to the boundary. For the cases where the plane wave propagates normal to the boundary, e^* and b^* are set to zero. For three-dimensional applications, Eqs.(2.33-2.34) can be expressed as:

$$\boldsymbol{F}\cdot\hat{n}=\begin{bmatrix}-n_yH_z+n_zH_y\\ n_xH_z-n_xH_z\\ -n_yH_z+n_zH_y\\ (B_zx_n-B_xz_n)z_n-(B_xy_n-B_yx_n)y_n\\ (B_xy_n-B_yx_n)x_n-(B_yz_n-B_zy_n)z_n\\ (B_yz_n-B_zy_n)y_n-(B_xy_n-B_yx_n)x_n\end{bmatrix} \tag{2.35}$$

For material jump boundary conditions (such as port boundaries and interface between different materials), the flux is determined using a Riemann solver:

$$\boldsymbol{F}(\boldsymbol{Q}_L,\boldsymbol{Q}_R)\cdot\hat{n}=\frac{1}{2}[\boldsymbol{F}(\boldsymbol{Q}_L)+\boldsymbol{F}(\boldsymbol{Q}_R)-[\tilde{T}][\tilde{\Lambda}][\tilde{T}][\widetilde{M}]\Delta\boldsymbol{Q}] \tag{2.36}$$

where $[\tilde{T}]$, $[\tilde{\Lambda}]$, and $[\widetilde{M}]$ represent average values and

$$\boldsymbol{Q}=(E_x,E_y,E_z,H_x,H_y,H_z)^T \tag{2.37}$$

And the difference in values across the interface $\Delta\boldsymbol{Q}$ can be expressed as:

$$\Delta\boldsymbol{Q}=\boldsymbol{Q}_R-\boldsymbol{Q}_L \tag{2.38}$$

Also, the matrix M is given by:

$$[M]=\left[\frac{\partial\boldsymbol{q}}{\partial\boldsymbol{Q}}\right] \tag{2.39}$$

Here, the flux densities $\boldsymbol{q}$ are computed at each mesh point during the simulations. The ideas above come from the flux-difference-splitting method in the fluid dynamic applications [68].

For port boundaries, the data on the interface is obtained from the field variables on each side, and driving wave is added on the interface of the excitation port. Duplicate

nodes are introduced in solving this problem and they are created on either side of the interface. The Riemann solver is also applied in this paper to simulate periodic boundary conditions.

The Floquet-Bloch periodic conditions are applied for simulation of photonic crystals. Its formulation is based on the knowledge of Riemann solver. The details of Floquet-Bloch periodic conditions will be discussed in detail in Chapter III in combination with the knowledge of photonic crystals.

Time-dependent Shape Sensitivity Analysis

In gradient-based optimization, sensitivity derivatives of the objective function are utilized to construct an appropriate search direction for improving the design. An automatic shape design cycle is implemented by combining an electromagnetics simulation codes, a time accurate adjoint based method for sensitivity analysis, a linear elasticity solver for mesh smoothing and an optimization package. In the current research the DAKOTA (Design Analysis Kit for Optimization and Terascale Applications) toolkit, developed at Sandia National Laboratories[69], is utilized. DAKOTA's optimization capabilities include a wide variety of gradient-based and nongradient-based optimization methods. It includes many external optimization libraries such as the OPT++ library[70], CONMIN and DOT libraries[71], and an interface to link with third-party routines that provide the function evaluations and sensitivity information. The optimization in current work is performed using a quasi-Newton method (from DAKOTA's OPT++ library). OPT++'s quasi-Newton method is based on the Broyden-Fletcher-Goldfard-Shanno (BFGS) [72] variable-metric algorithm. Opt++'s quasi-Newton method uses a line searching approach based on the algorithm by More and Thuente [73].

The objective of the shape design cycle is to minimize the cost function for realizing desired characteristics by modifying the shape of the optical structure. In the discussions below, the cost function is denoted as $costI$, and the design variable is denoted as β. The methods for computing the sensitivities and surface parameterization utilized in current work will be discussed in the following sections.

Sensitivity Analysis

Finite Difference Method

The derivative of the cost function with respect to the design variable can be approximated by the central-difference method expressed as:

$$\frac{\partial costI}{\partial \beta} = \frac{costI(\beta+\Delta\beta)-costI(\beta-\Delta\beta)}{2\Delta\beta} + O(\Delta\beta^2) \tag{2.40}$$

The central finite-difference method is subject to subtractive cancellation, and the truncation error increases as $\Delta\beta$ decreases. This method is utilized as a tool for accuracy verification in current work. It is not practical when multiple design variables are used to design an object since it requires two highly-converged solutions for each design variable.

Forward Mode Direct Differentiation

The sensitivity derivative can be computed using a forward mode direct differentiation by examining the functional dependencies of the cost function. The cost function is defined as:

$$costI = costI(\beta, X, q) \tag{2.41}$$

where the dependencies are the design variables β, computational mesh X and the solution quantities q. The total differential of the cost function with respect to the design variable is given by:

$$\frac{dcostI}{d\beta} = \frac{\partial costI}{\partial \beta} + \frac{\partial costI}{\partial X}\frac{\partial X}{\partial \beta} + \frac{\partial costI}{\partial q}\frac{\partial q}{\partial \beta} \tag{2.42}$$

The residual of the governing equation for a time-dependent problem at i^{th} time step, BDF2 in this case, can be expressed as:

$$R^i\left(\beta, X, q^i, q^{i-1}, q^{i-2}\right) = 0 \tag{2.43}$$

Therefore the total differential of residual with respect to β at time step i is given by:

$$\frac{dR^i}{d\beta} = \frac{\partial R^i}{\partial \beta} + \frac{\partial R^i}{\partial X}\frac{\partial X}{\partial \beta} + \frac{\partial R^i}{\partial q^i}\frac{\partial q^i}{\partial \beta} + \frac{\partial R^i}{\partial q^{i-1}}\frac{\partial q^{i-1}}{\partial \beta} + \frac{\partial R^i}{\partial q^{i-2}}\frac{\partial q^{i-2}}{\partial \beta} = 0 \tag{2.44}$$

Then the derivative of solution quantities with respect to design variable at i^{th} time step is obtained by:

$$\frac{\partial q^i}{\partial \beta} = -\left[\frac{\partial R^i}{\partial q^i}\right]^{-1}\left(\frac{\partial R^i}{\partial X}\frac{\partial X}{\partial \beta} + \frac{\partial R^i}{\partial q^{i-1}}\frac{\partial q^{i-1}}{\partial \beta} + \frac{\partial R^i}{\partial q^{i-2}}\frac{\partial q^{i-2}}{\partial \beta}\right) \tag{2.45}$$

By applying Eq.(2.45) into Eq.(2.42), the sensitivity derivative for time-dependent problems using the forward mode direct differentiation is given by:

$$\frac{dcostI}{d\beta} = \frac{\partial costI}{\partial \beta} + \frac{\partial costI}{\partial X}\frac{\partial X}{\partial \beta} - \sum_{i=1}^{ncyc}\frac{\partial costI}{\partial q^i}\left[\frac{\partial R^i}{\partial q^i}\right]^{-1}\left(\frac{\partial R^i}{\partial X}\frac{\partial X}{\partial \beta} + \frac{\partial R^i}{\partial q^{i-1}}\frac{\partial q^{i-1}}{\partial \beta} + \frac{\partial R^i}{\partial q^{i-2}}\frac{\partial q^{i-2}}{\partial \beta}\right) \tag{2.46}$$

where $ncyc$ is the total number of time steps. The forward mode, direct differentiation method is not practical for shape design problems with multiple design variables, since the computational costs scale with the number of design variables. In current work, the direct sensitivity is used as a comparison tool for the reverse mode discrete adjoint formulation.

Reverse Mode Discrete Adjoint Formulation

The reverse mode discrete adjoint formulation is efficient for computing sensitivity derivatives for problems with multiple design variables. The adjoint formulation eliminates the computational overhead caused by repetitive calculations of the solution sensitivities by transposing the inverse of the Jacobian matrix. The third term in Eq.(2.46) can be expressed as:

$$\begin{aligned}&\sum_{i=1}^{ncyc}\frac{\partial costI}{\partial q^i}\left[\frac{\partial R^i}{\partial q^i}\right]^{-1}\left(\frac{\partial R^i}{\partial X}\frac{\partial X}{\partial \beta}+\frac{\partial R^i}{\partial q^{i-1}}\frac{\partial q^{i-1}}{\partial \beta}+\frac{\partial R^i}{\partial q^{i-2}}\frac{\partial q^{i-2}}{\partial \beta}\right)\\&=\sum_{i=1}^{ncyc}\left[\lambda_q^i\right]^T\left(\frac{\partial R^i}{\partial X}\frac{\partial X}{\partial \beta}+\frac{\partial R^i}{\partial q^{i-1}}\frac{\partial q^{i-1}}{\partial \beta}+\frac{\partial R^i}{\partial q^{i-2}}\frac{\partial q^{i-2}}{\partial \beta}\right)\\&=\sum_{i=1}^{ncyc}\left(\left[\lambda_q^i\right]^T\frac{\partial R^i}{\partial X}\frac{\partial X}{\partial \beta}+\left[\psi_1^i\right]^T\frac{\partial q^{i-1}}{\partial \beta}+\left[\psi_2^i\right]^T\frac{\partial q^{i-2}}{\partial \beta}\right)\end{aligned}\tag{2.47}$$

where

$$\lambda_q^i=\left[\frac{\partial R^i}{\partial q^i}\right]^{-T}\left[\frac{\partial costI}{\partial q^i}\right]^T\tag{2.48}$$

$$\psi_1^i=\left[\frac{\partial R^i}{\partial q^{i-1}}\right]^T\lambda_q^i\tag{2.49}$$

$$\psi_2^i=\left[\frac{\partial R^i}{\partial q^{i-2}}\right]^T\lambda_q^i\tag{2.50}$$

As observed from Eq.(2.47), the solution sensitivities from the earlier two time steps are not available in adjoint mode. To avoid the evolution of unavailable terms, the adjoint variables of newer time steps can be regrouped with the ones of older time steps. Then the reformulated adjoint variable becomes:

$$\lambda_q^i=\left[\frac{\partial R^i}{\partial q^i}\right]^{-T}\left(\left[\frac{\partial costI}{\partial q^i}\right]^T+\left[\psi_1^{i+1}\right]^T+\left[\psi_2^{i+2}\right]^T\right)\tag{2.51}$$

The total differential of the objective function in terms of the adjoint vector is expressed as:

$$\frac{dcostI}{d\beta}=\frac{\partial costI}{\partial \beta}+\frac{\partial costI}{\partial X}\frac{\partial X}{\partial \beta}+\left[\lambda_q^i\right]^T\left(\frac{\partial R^i}{\partial X}\frac{\partial X}{\partial \beta}\right)\tag{2.52}$$

Once the sensitivity derivatives of the objective function are evaluated, they are utilized to predict an appropriate search direction. The basic algorithm can be written as:

Algorithm. A discrete adjoint formulation for time-dependent sensitivity derivatives

(1)Set ψ_1^{i+1},ψ_2^{i+1},$\psi_2^{i+2}$to be zero. Set i to be ncyc.

(2)Solve Eq. (2.51) for the adjoint variable.

(3)Set the sensitivity derivatives by Eq. (2.52).

(4)Set $\psi_2^{i+2} = \psi_2^{i+1}$.

(5)Set $i = i - 1$.

(6)Solve Eqs. (2.49-2.50) for ψ_1^{i+1} and ψ_2^{i+1}.

(7)If $i = 1$, stop; otherwise go to step 2.

Surface Parameterization

During a design cycle the geometry is modified through surface node displacements according to a defined parameterization. The specific method will dictate the set of geometric design variables. In current work, surface parameterization methods of Bezier Curves and Hicks-Henne functions are utilized, Linear-Elastic smoothing is applied to move interior mesh points in response to boundary movement. The surface parameterization methods and mesh smoothing methods will be discussed in the following sections.

Linear-Elastic Smoothing

For current work, sensitivity analysis is applied for two-dimensional applications only, and the following discussions will focus on two-dimensional cases. The Linear-

Elastic equations represent the perturbation field on the inside of the domain based on the perturbations prescribed on the boundaries, and are given by[74]:

$$\frac{\partial}{\partial x}\left[\alpha_{11}\frac{\partial \Delta x}{\partial x}\right]+\frac{\partial}{\partial y}\left[\alpha_{12}\frac{\partial \Delta x}{\partial y}\right]+\frac{\partial}{\partial x}\left[\theta_{11}\frac{\partial \Delta y}{\partial y}\right]+\frac{\partial}{\partial y}\left[\theta_{12}\frac{\partial \Delta y}{\partial x}\right]=0 \tag{2.53}$$

$$\frac{\partial}{\partial x}\left[\alpha_{21}\frac{\partial \Delta y}{\partial x}\right]+\frac{\partial}{\partial y}\left[\alpha_{22}\frac{\partial \Delta y}{\partial y}\right]+\frac{\partial}{\partial x}\left[\theta_{21}\frac{\partial \Delta x}{\partial y}\right]+\frac{\partial}{\partial y}\left[\theta_{22}\frac{\partial \Delta x}{\partial x}\right]=0 \tag{2.54}$$

Here Δx and Δy are the displacements of the x and y coordinates. The coordinates of interior nodes are updated by:

$$x_{new}=x_{old}+\Delta x \tag{2.55}$$

$$y_{new}=y_{old}+\Delta y \tag{2.56}$$

The parameters in Eqs.(2.53-2.54) are defined as:

$$\alpha_{11}=\alpha_{22}=\frac{E}{1-\nu^2} \tag{2.57}$$

$$\alpha_{12}=\alpha_{21}=\theta_{12}=\theta_{21}=\frac{E}{2(1+\nu)} \tag{2.58}$$

$$\theta_{11}=\theta_{22}=\frac{\nu E}{1-\nu^2} \tag{2.59}$$

where ν is Poisson's Ratio, and E is Young's Modulus.

The Linear-Elastic equations are solved with the Galerkin finite element method given by:

$$\frac{\partial \boldsymbol{F}_{LE}}{\partial x}+\frac{\partial \boldsymbol{G}_{LE}}{\partial y}=0 \tag{2.60}$$

where

$$\boldsymbol{q}_{LE}=\begin{bmatrix}\Delta x\\ \Delta y\end{bmatrix} \tag{2.61}$$

$$\boldsymbol{F}_{LE}=\begin{bmatrix}\alpha_{11}\frac{\partial \Delta x}{\partial x}+\theta_{11}\frac{\partial \Delta y}{\partial y}\\ \alpha_{21}\frac{\partial \Delta y}{\partial x}+\theta_{21}\frac{\partial \Delta x}{\partial y}\end{bmatrix} \tag{2.62}$$

$$\boldsymbol{G}_{LE} = \begin{bmatrix} \alpha_{12}\frac{\partial \Delta x}{\partial y} + \theta_{12}\frac{\partial \Delta y}{\partial x} \\ \alpha_{22}\frac{\partial \Delta y}{\partial y} + \theta_{22}\frac{\partial \Delta x}{\partial x} \end{bmatrix} \tag{2.63}$$

The governing equations in weak form are expressed as:

$$\int_{\Omega} w\left(\frac{\partial \boldsymbol{F}}{\partial x} + \frac{\partial \boldsymbol{Q}}{\partial y}\right)\partial\Omega = 0 \tag{2.64}$$

The Linear-Elastic equations are solved in matrix form as:

$$[M][\boldsymbol{q}_{LE}] = [RHS] \tag{2.65}$$

where $[M]$ is the stiffness matrix for solving the resulting mesh movement. To calculate the mesh sensitivity derivatives, the following equations in matrix form will be solved:

$$[M]\left[\frac{\partial \boldsymbol{q}_{LE}}{\partial \beta}\right] = \left[\frac{\partial RHS}{\partial \beta}\right] \tag{2.66}$$

Hicks-Henne Function

The Hicks-Henne sine bump function is utilized to ensure smooth surface shape, given by:

$$b_i(x_{si}, \beta_m) = \beta_m sin^4\left(\pi x_{si}^{\ln(0.5)/\ln(x_{sm})}\right) \tag{2.67}$$

where the design variables are set to be the magnitudes of the bump functions $\boldsymbol{\beta} = \{\beta_m, m = 1, \cdots, N_d\}$. In Eq.(2.67), b_i represents the surface node displacement at x_{si} due to the displacement of the surface node at x_{sm}, and β_m denotes the m^{th} component of the design variables associated with the surface node at x_{sm}. The modified surface coordinates are computed by:

$$x_{si}^{new} = x_{si}^{old} + \sum_{m=1}^{ndv} b_i(x_{si}, \beta_m) \tag{2.68}$$

where ndv represents the total number of design variables.

Bezier Curve

A Bezier curve is defined by a set of control points $\boldsymbol{P}_0$ through $\boldsymbol{P}_n$, and n is the curve's order. The first and last control points are the start and end points of the curve, respectively. The intermediate control points generally do not lie on the curve. A Bezier curve can be expressed as:

$$\boldsymbol{B}(t) = \sum_{i=0}^{n} \boldsymbol{P}_i \frac{n!}{i!(n-i)!} t^i (1-t)^{n-i} \tag{2.69}$$

where $0 \leq t \leq 1$, and t represents the position of design points. $\boldsymbol{P}_i$ are control points for the Bezier curve, and we have:

$$\boldsymbol{B}(t) = \begin{bmatrix} x_{Bezier}(t) \\ y_{Bezier}(t) \end{bmatrix} \tag{2.70}$$

$$\boldsymbol{P_i} = \begin{bmatrix} x_{control}(i) \\ y_{control}(i) \end{bmatrix} \tag{2.70}$$

The setting of design variables needs to be combined with real design problems and will be discussed in more detail in Chapter IV.

CHAPTER III

PHOTONIC CRYSTALS: THEORY, SIMULATION AND RESULTS

Introduction

Photonic crystals are composed of periodic structures that affect electromagnetic wave propagation in the same way that the periodic potential in a semiconductor crystal affects electron motion by defining allowed and forbidden electronic energy bands. This periodicity is the electromagnetic analogue of a crystalline atomic lattice[2]. That is where the name "crystal" comes from.

Photonic crystals contain regularly repeating regions of high and low dielectric constant. Whether waves propagate through this structure or not depends on their wavelength. Wavelengths that don't propagate form disallowed bands called photonic band gaps.

The dispersion relation (band diagram) of the photonic crystal describes the location and size of the photonic band gap (PBG). The knowledge of Floquet-Bloch periodic conditions and Brillouin zone are utilized in calculating the PBG. The methods for computing the band diagram of the photonic crystals with lattice types of both square lattice and triangular lattice are discussed in the following sections. In current work, we focus on the simulation of two-dimensional photonic crystals.

Calculation of Band Diagram

A two-dimensional photonic crystal is periodic along two of its axes and homogeneous along the third axis. Within the photonic crystal, one basic configuration unit (the unit cell) is replicated over and over corresponding to a periodic dielectric function $\varepsilon(\boldsymbol{r}) = \varepsilon(\boldsymbol{r} + \boldsymbol{R})$. According to Bloch's theorem, the electromagnetic mode can be expressed as a plane wave that is modulated by a periodic function $u(\boldsymbol{r}) = u(\boldsymbol{r} + \boldsymbol{R})$, where the function $u(\boldsymbol{r})$ shares the same periodicity as the photonic crystal.

Floquet-Bloch Periodic Conditions

The simulation is run on the unit cell with Floquet-Bloch periodic conditions applied on the boundaries. The expressions of Floquet-Bloch periodic conditions depend on the lattice type (periodic function $u(\boldsymbol{r})$) of the photonic crystal. The two most used lattice types: square lattice and triangular lattice are discussed in the following sections.

Square Lattice

The proposed photonic crystal is made of cylinders of refractive index n_1 immersed in a medium of refractive index n_2. As shown in Fig. 3.1(a), the cylinders are repeated with periodicity of the lattice constant a along both x and y directions. The computational geometry of the unit cell is shown in Fig. 3.1(b).

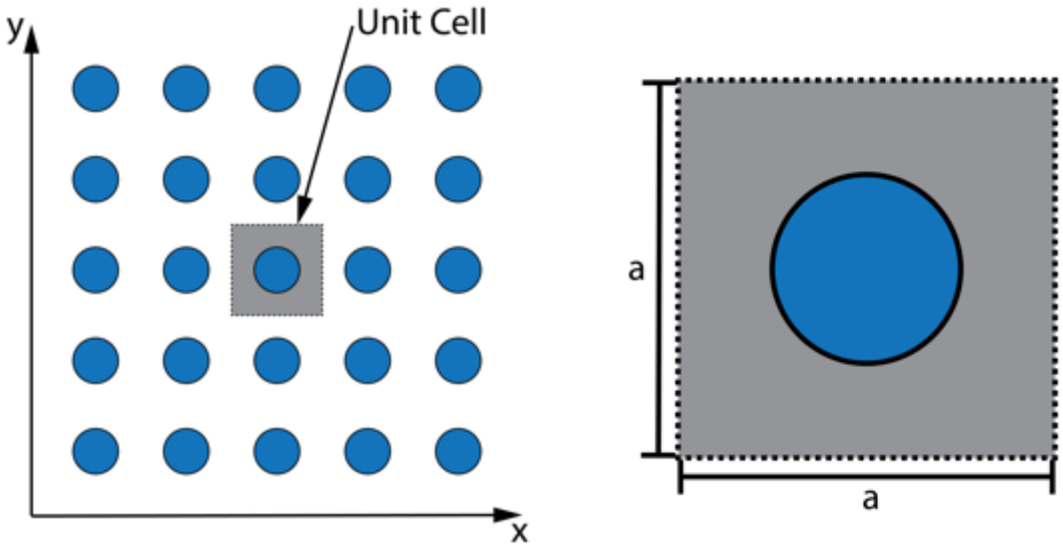

a) 2D photonic crystal: square lattice b) Unit cell

Figure 3.1 Square lattice structure and unit cell

For square lattice with the given unit cell, the Floquet-Bloch periodic conditions applied to the electric and magnetic components are shown in Eqs.(3.1-3.4). In the equations, a is the lattice constant and k_x, k_y are the wave numbers. The selection of the values of k_x and k_y will be discussed in detail later in this chapter.

$$E(x = 0, y, t) = E(x = a, y, t)\exp(-ik_x \cdot a) \quad (3.1)$$

$$E(x, y = 0, t) = E(x, y = a, t)\exp(-ik_y \cdot a) \quad (3.2)$$

$$H(x = a, y, t) = H(x = 0, y, t)\exp(ik_x \cdot a) \quad (3.3)$$

$$H(x, y = a, t) = H(x, y = 0, t)\exp(ik_y \cdot a) \quad (3.4)$$

Triangular Lattice

The periodic structure of the triangular lattice and the simulation geometry of the unit cell are shown in Fig. 3.2. For triangular lattice with the given unit cell, the Floquet-Bloch conditions applied to the electric and magnetic components are shown in Eq.(3.5-3.10). As shown in Fig. 3.2(b), there are three pairs of periodic conditions. Equations

(3.5-3.6) are applied on the boundaries of $x = 0$ and $x = a$. Equations (3.7-3.8) are applied on the boundaries of $0 \le x \le a/2, y = 0$ and $a/2 \le x \le a, y = b$ illustrated by the black arrow in Fig. 3.2(b), and Equations (3.9-3.10) are applied on the boundaries of $a/2 \le x \le a, y = 0$ and $0 \le x \le a/2, y = b$ illustrated by the red arrow in Fig. 3.2(b), where $b = \frac{\sqrt{3}}{2}$a.

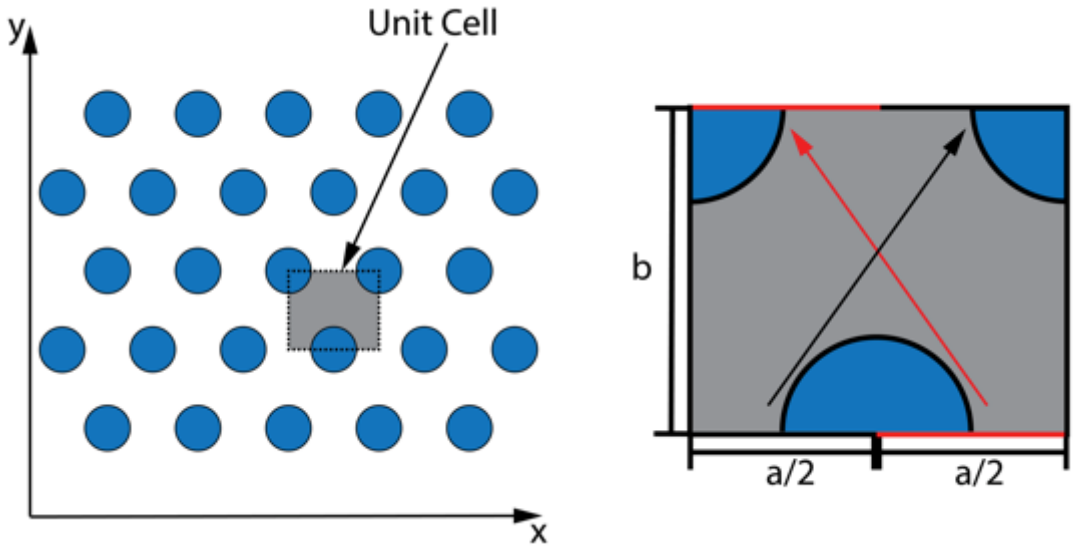

a) 2D photonic crystal: triangular lattice b) Unit cell

Figure 3.2 Triangular lattice structure and unit cell

$$E(x = 0, y, t) = E(x = a, y, t)\exp(-ik_x \cdot a) \tag{3.5}$$

$$H(x = a, y, t) = H(x = 0, y, t)\exp(ik_x \cdot a) \tag{3.6}$$

$$E(x, y = 0, t) = E\left(x + \frac{a}{2}, y = \frac{\sqrt{3}}{2}a, t\right)\exp(-ik_y \cdot \frac{\sqrt{3}}{2}a - ik_x \cdot \frac{a}{2}) \tag{3.7}$$

$$H\left(x, y = \frac{\sqrt{3}}{2}a, t\right) = H\left(x + \frac{a}{2}, y = 0, t\right)\exp(ik_y \cdot \frac{\sqrt{3}}{2}a - ik_x \cdot \frac{a}{2}) \tag{3.8}$$

$$E(x, y = 0, t) = E\left(x - \frac{a}{2}, y = \frac{\sqrt{3}}{2}a, t\right)\exp\left(-ik_y \cdot \frac{\sqrt{3}}{2}a + ik_x \cdot \frac{a}{2}\right) \tag{3.9}$$

$$H\left(x, y = \frac{\sqrt{3}}{2}a, t\right) = H\left(x - \frac{a}{2}, y = 0, t\right)\exp(ik_y \cdot \frac{\sqrt{3}}{2}a + ik_x \cdot \frac{a}{2}) \tag{3.10}$$

To realize the Floquet-Bloch periodic conditions in the code, the original Riemann solver is modified by adding a factor that is a complex number related to the wave vector. Since the periodic boundaries are considered as duplicate edges in the code, the mesh points on the paired boundaries must be identical.

Reciprocal Lattice and Brillouin Zone

According to the knowledge of solid-state physics[75], only wave vectors $\boldsymbol{k}$ that lie in the irreducible Brillouin zone need to be considered to get enough information for the band diagram. To introduce Brillouin zone, reciprocal lattice must be discussed first.

By taking Fourier transform of the periodic function $u(\boldsymbol{r}) = u(\boldsymbol{r} + \boldsymbol{R})$, we have:

$$g(\boldsymbol{k}) = g(\boldsymbol{k}) * \exp(i\boldsymbol{k} \cdot \boldsymbol{R}) \tag{3.11}$$

where $g(\boldsymbol{k})$ is the Fourier transform of $u(\boldsymbol{r})$, and it is the coefficient on the plane wave with the vector $\boldsymbol{k}$. To satisfy Eq.(3.11), we must have either $g(\boldsymbol{k}) = 0$ or $\exp(i\boldsymbol{k} \cdot \boldsymbol{R}) = 1$. That means, $g(\boldsymbol{k})$ is zero everywhere, except for spikes at the values of $\boldsymbol{k}$ such that $\exp(i\boldsymbol{k} \cdot \boldsymbol{R}) = 1$ for all $\boldsymbol{R}$.

The vectors $\boldsymbol{k}$ which satisfies $\exp(i\boldsymbol{k} \cdot \boldsymbol{R}) = 1$ or $\boldsymbol{k} \cdot \boldsymbol{R} = 2\pi N$, are called reciprocal lattice vectors. The reciprocal lattice vectors are usually designated by the letter $\boldsymbol{G}$ and they form a lattice of their own. Every lattice vector $\boldsymbol{R}$ can be written in terms of the primitive lattice vectors as:

$$\boldsymbol{R} = l_R \boldsymbol{a}_1 + m_R \boldsymbol{a}_2 + n_R \boldsymbol{a}_3 \tag{3.12}$$

Similarly, the reciprocal lattice vectors can be written in terms of their primitive lattice vectors as:

$$\boldsymbol{G} = l_G \boldsymbol{b}_1 + m_G \boldsymbol{b}_2 + n_G \boldsymbol{b}_3 \tag{3.13}$$

Then, the lattice vector $\boldsymbol{R}$ and $\boldsymbol{G}$ need to satisfy:

$$\boldsymbol{G}\cdot\ \boldsymbol{R} = (l_R\boldsymbol{a}_1 + m_R\boldsymbol{a}_2 + n_R\boldsymbol{a}_3)\cdot(l_G\boldsymbol{b}_1 + m_G\boldsymbol{b}_2 + n_G\boldsymbol{b}_3) = \ 2\pi N \qquad (3.14)$$

For all choices of (l, m, n), Eq.(3.14) must hold for some *N*. To satisfy that, we will have $\boldsymbol{a}_i \cdot \boldsymbol{b}_j = 2\pi\delta_{ij}$. Based on these relationships, to construct the primitive reciprocal lattice vectors in terms of the primitive lattice vectors, we have:

$$\boldsymbol{b}_1 = \frac{2\pi\boldsymbol{a}_2\times\boldsymbol{a}_3}{\boldsymbol{a}_1\cdot(\boldsymbol{a}_2\times\boldsymbol{a}_3)} \qquad (3.15)$$

$$\boldsymbol{b}_2 = \frac{2\pi\boldsymbol{a}_3\times\boldsymbol{a}_1}{\boldsymbol{a}_1\cdot(\boldsymbol{a}_2\times\boldsymbol{a}_3)} \qquad (3.16)$$

$$\boldsymbol{b}_3 = \frac{2\pi\boldsymbol{a}_1\times\boldsymbol{a}_2}{\boldsymbol{a}_1\cdot(\boldsymbol{a}_2\times\boldsymbol{a}_3)} \qquad (3.17)$$

After taking the Fourier transform of a function that is periodic on a lattice, only the terms with wave vectors that are reciprocal lattice vectors need to be included.

The electromagnetic modes can be written in Bloch form, since the translational symmetry of a photonic crystal allows us to classify the electromagnetic modes with a wave vector $\boldsymbol{k}$. In Bloch form, the plane wave is modulated by a function that shares the periodicity of the lattice. In Bloch states, a mode with wave vector $\boldsymbol{k}$ and a mode with wave vector $\boldsymbol{k}+\boldsymbol{G}$ are the same mode, if $\boldsymbol{G}$ is a reciprocal lattice vector. Then, we can restrict calculation to a finite zone in reciprocal space, where all values of $\boldsymbol{k}$ that lie outside this zone can be reached from within the zone. Among such zones, we will focus on the one closest to $\boldsymbol{k}$=0. This zone is the (first) Brillouin zone.

In the following sections, the reciprocal lattice and Brillouin zone of square lattice and triangular lattice will be discussed in detail.

Square Lattice

Figure 3.3(a) shows the structure of square lattice. For a square lattice with lattice constant a, the lattice vectors are respectively: $\boldsymbol{a}_1 = a\boldsymbol{x}$, $\boldsymbol{a}_2 = a\boldsymbol{y}$ and $\boldsymbol{a}_3 = l\boldsymbol{z}$, where l

can be any length. By putting the lattice vectors into Eq.(3.15-3.17), the reciprocal lattice vectors are obtained, they are $\boldsymbol{b}_1 = (2\pi/a)\boldsymbol{x}$ and $\boldsymbol{b}_2 = (2\pi/a)\boldsymbol{y}$. The corresponding reciprocal lattice is shown in Fig. 3.3(b), and it is a square lattice with reciprocal lattice constant of $2\pi/a$.

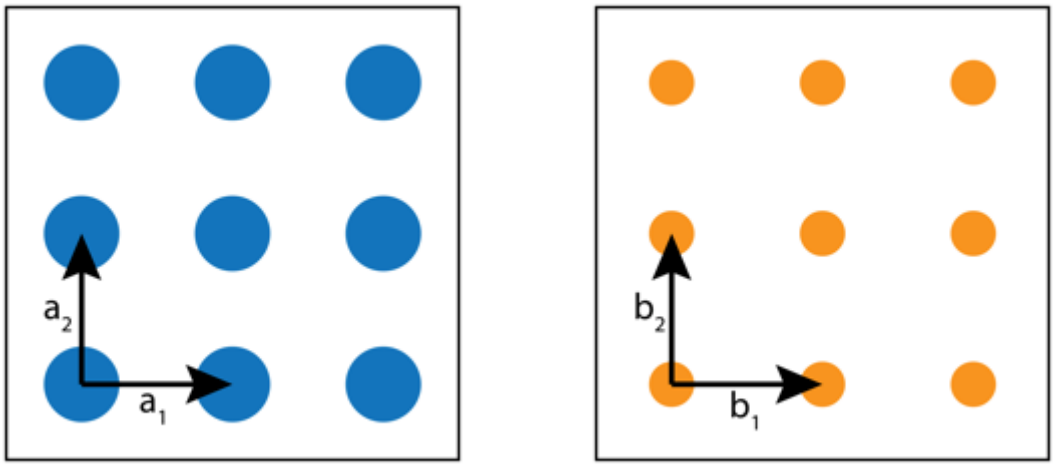

(a) Real lattice (b) Reciprocal lattice

Figure 3.3 The real and reciprocal lattice of the square lattice

Fig. 3.4(a) is the construction of the first Brillouin zone: taking the center point as the origin, connecting the lines from the origin to the other lattice points, getting their perpendicular bisectors, and the square boundary of the Brillouin zone is obtained. As shown in Fig. 3.4(b), in the irreducible Brillouin zone, the coordinates of the points Γ, X, M are $(0,0), (\pi/a, 0), (\pi/a, \pi/a)$, respectively. The band diagram will be calculated along the triangular edge of the irreducible Brillouin zone, from Γ to X to M.

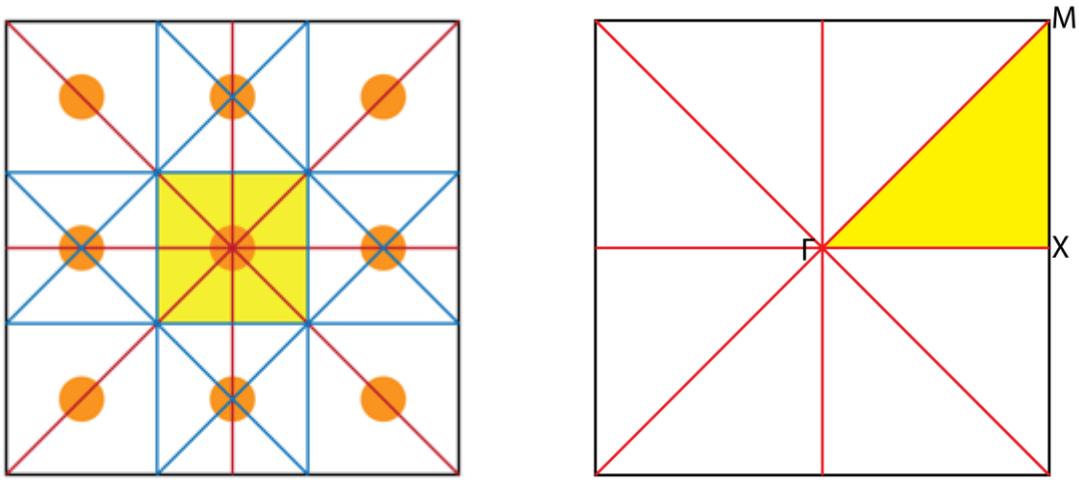

(a) Brillouin zone (b) Irreducible Brillouin zone

Figure 3.4 The Brillouin zone and irreducible Brillouin zone of the square lattice

The coordinates of points in the irreducible Brillouin zone are the wave vectors k_x, k_y for the Floquet-Bloch conditions. In current work, we pick 15 points along the edge of the irreducible Brillouin zone, x and y coordinates of each points which are also the wave vectors k_x, k_y are shown in Table 3.1, where the point ΓnX represents the nth point between the node Γ and X, same for XnM and MnΓ. The wave vectors are put into Eq.(3.1-3.4) and then form 15 different boundary conditions.

Table 3.1. Wave Vectors in the Irreducible Brillouin Zone of Square Lattice

	Γ	Γ1X	Γ2X	Γ3X	Γ4X
k_x	0	$0.2\pi/a$	$0.4\pi/a$	$0.6\pi/a$	$0.8\pi/a$
k_y	0	0	0	0	0
	X	X1M	X2M	X3M	X4M
k_x	π/a	π/a	π/a	π/a	π/a

k_y	0	$0.2\pi/a$	$0.4\pi/a$	$0.6\pi/a$	$0.8\pi/a$
	M	M1Γ	M2Γ	M3Γ	M4Γ
k_x	π/a	$0.8\pi/a$	$0.6\pi/a$	$0.4\pi/a$	$0.2\pi/a$
k_y	π/a	$0.8\pi/a$	$0.6\pi/a$	$0.4\pi/a$	$0.2\pi/a$

Triangular Lattice

Figure 3.5(a) shows the structure of triangular lattice. For a triangular lattice with lattice constant a, the lattice vectors are respectively: $\boldsymbol{a}_1 = \frac{a}{2}(\boldsymbol{x} + \sqrt{3}\boldsymbol{y})$, $\boldsymbol{a}_2 = \frac{a}{2}(\boldsymbol{x} - \sqrt{3}\boldsymbol{y})$ and $\boldsymbol{a}_3 = l\boldsymbol{z}$, where l can be any length. By putting the lattice vectors into Eqs.(3.15-3.17), the reciprocal lattice vectors are obtained, they are $\boldsymbol{b}_1 = (2\pi/a)(\boldsymbol{x} + \frac{\mathbf{1}}{\sqrt{\mathbf{3}}}\boldsymbol{y})$ and $\boldsymbol{b}_2 = (2\pi/a)(\boldsymbol{x} - \frac{\mathbf{1}}{\sqrt{\mathbf{3}}}\boldsymbol{y})$. The corresponding reciprocal lattice is shown in Fig. 3.5(b), and it is a triangular lattice with reciprocal lattice constant of $4\pi/\sqrt{3}a$ and a rotation of 90 degree with respect to the real lattice.

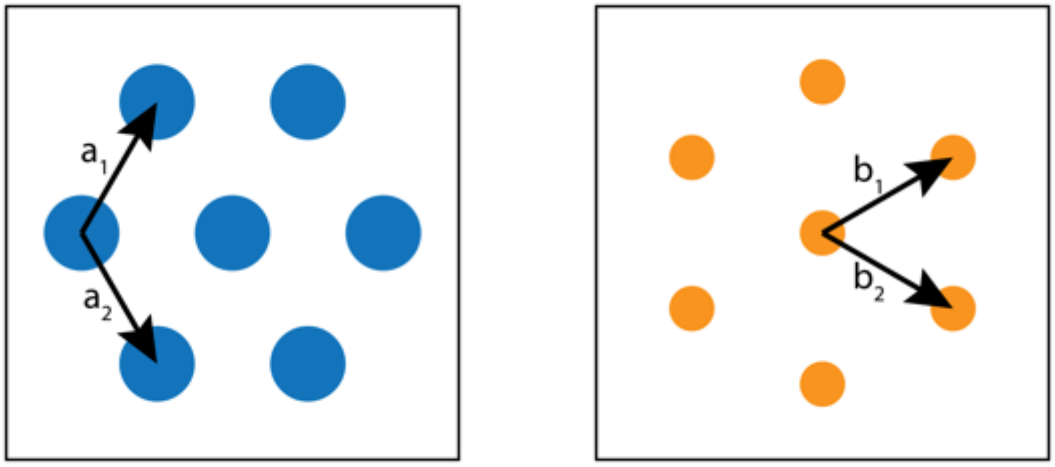

(a) Real lattice (b) Reciprocal lattice

Figure 3.5 The real and reciprocal lattice of the triangular lattice

Fig. 3.6(a) is the construction of the first Brillouin zone, which is a hexagon centered on the origin. As shown in Fig. 3.6(b), in the irreducible Brillouin zone, the coordinates of the points Γ, M, X are $(0,0), \left(0, 2\pi/\sqrt{3}a\right), \left(2\pi/3a, 2\pi/\sqrt{3}a\right)$,respectively. The band diagram will be calculated along the triangular edge of the irreducible Brillouin zone, from Γ to M to X. The coordinates of points in the irreducible Brillouin zone are the wave vectors k_x, k_y for the Floquet-Bloch conditions. In current work, we pick 15 points along the edge of the irreducible Brillouin zone, x and y coordinates of each points which are also the wave vectors k_x, k_y are shown in Table 3.2. By applying the wave vectors into Eq.(3.5-3.10), 15 different boundary conditions are formed.

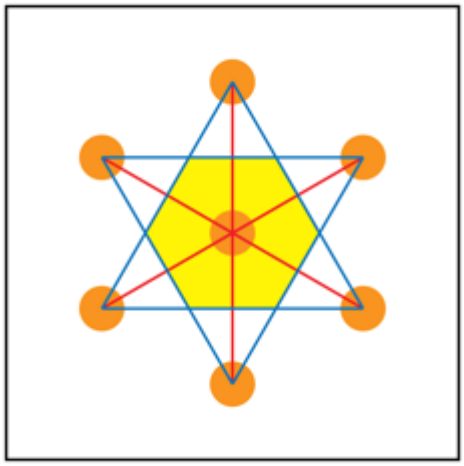

(a) Brillouin zone (b) Irreducible Brillouin zone

Figure 3.6 The Brillouin zone and irreducible Brillouin zone of the triangular lattice

Table 3.2. Wave Vectors in the Irreducible Brillouin Zone of Triangular Lattice

	Γ	Γ1M	Γ2M	Γ3M	Γ4M
k_x	0	0	0	0	0
k_y	0	$0.4\pi/\sqrt{3}a$	$0.8\pi/\sqrt{3}a$	$1.2\pi/\sqrt{3}a$	$1.6\pi/\sqrt{3}a$
	M	M1X	M2X	M3X	M4X
k_x	0	$0.4\pi/3a$	$0.8\pi/3a$	$1.2\pi/3a$	$1.6\pi/3a$
k_y	$2\pi/\sqrt{3}a$	$2\pi/\sqrt{3}a$	$2\pi/\sqrt{3}a$	$2\pi/\sqrt{3}a$	$2\pi/\sqrt{3}a$
	X	X1Γ	X2Γ	X3Γ	X4Γ
k_x	$2\pi/3a$	$1.6\pi/3a$	$1.2\pi/3a$	$0.8\pi/3a$	$0.4\pi/3a$
k_y	$2\pi/\sqrt{3}a$	$1.6\pi/\sqrt{3}a$	$1.2\pi/\sqrt{3}a$	$0.8\pi/\sqrt{3}a$	$0.4\pi/\sqrt{3}a$

Excitation and Monitoring

In simulation of the unit cell of photonic crystals, source points and monitoring points are chosen randomly[76]. At the source points, a modulated Gaussian pulse is applied to excite the electromagnetic modes over a wide range of frequencies, and the formulation is shown as follow[77]:

$$V = cost(\omega(t - t_0))e^{-\frac{(t-t_0)^2}{a}} \tag{3.18}$$

$$a = \frac{\sqrt{2.3}}{\pi f_{max}} \tag{3.19}$$

$$t_0 = \sqrt{m}a \tag{3.20}$$

where V represents the value of Gaussian pulse, t_0 and m can be used to control the delay of the source waveform.

While running the simulation, we record the temporal response at the monitoring points at each time step until the solution has converged. Then we take a Fourier transform of the temporal results to obtain the frequency spectra where peaks at certain frequencies can be observed. Then these frequencies where the peaks are located are plotted on the band diagram for wave vector $\boldsymbol{k}$. By looping all the wave vectors from the irreducible Brillouin zone, that means changing the wave vector $\boldsymbol{k}$ in the Floquet-Bloch boundary condition for each simulation, we will get the entire band diagram.

Simulation Results of Photonic Band Gaps

Square Lattice

The first test case is to simulate the light propagation in the $x\sim y$ plane of a square array of dielectric columns as shown in Fig. 3.1, with lattice constant $a = 200nm$. The proposed photonic crystal consists of silicon $(\varepsilon = 12.0)$ rods in air, with radius $r = 40nm$.

The simulation is run on the unit cell shown in Fig. 3.1(b) over a frequency range of 0-150THz in TM mode with 15 different boundary conditions mentioned in last section. Fourier transform of the temporal response of z-component of electric field at 15 different wave vectors $\boldsymbol{k}$ are shown in Fig. 3.7(a-o). The band diagram is obtained by applying a peak finding function at each frequency spectra, and the resulting band diagram is shown in Fig. 3.8. The frequency on the vertical axis is expressed as normalized frequency fa/c, and the horizontal axis shows the value of the in-plane wave vector $\boldsymbol{k}$. As we move from left the right, $\boldsymbol{k}$ moves along the triangular edge of the irreducible Brillouin zone, from Γ to X to M, as shown in Fig. 3.4(b). The simulation result of band diagram is compared with MPB[78], the results match each other well. As illustrated in Fig. 3.8, the band gap of the proposed photonic crystal is from 420THz to 620THz.

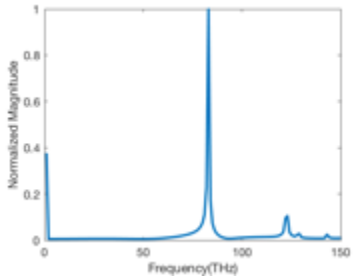

(a) $k_x = 0.0, k_y = 0.0$

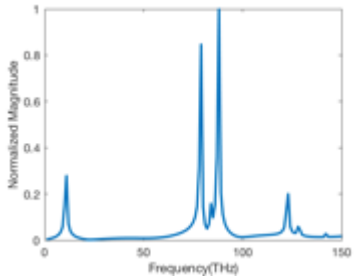

(b) $k_x = 0.2\pi/a, k_y = 0.0$

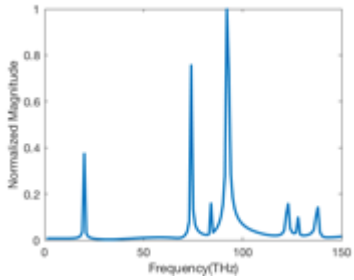

(c) $k_x = 0.4\pi/a, k_y = 0.0$

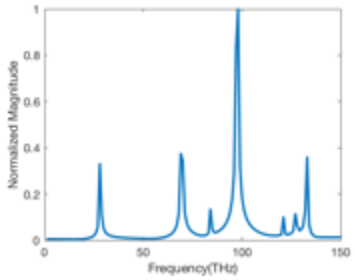

(d) $k_x = 0.6\pi/a, k_y = 0.0$

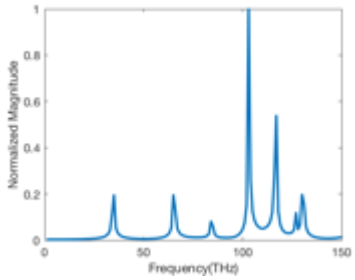

(e) $k_x = 0.8\pi/a, k_y = 0.0$

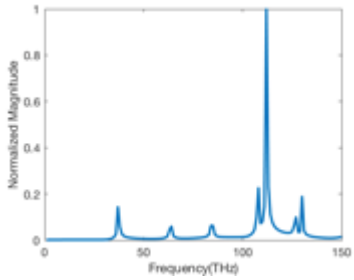

(f) $k_x = \pi/a, k_y = 0.0$

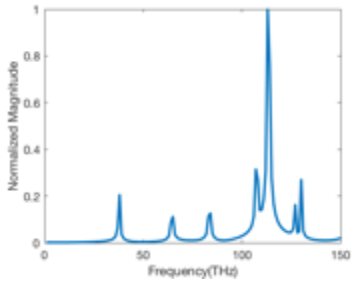

(g) $k_x = \pi/a, k_y = 0.2\pi/a$

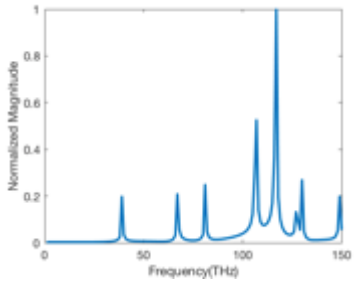

(h) $k_x = \pi/a, k_y = 0.4\pi/a$

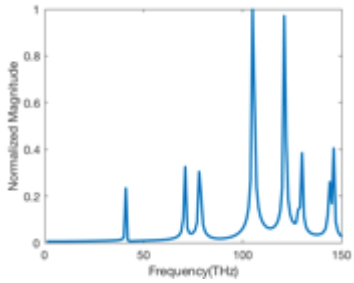

(i) $k_x = \pi/a, k_y = 0.6\pi/a$

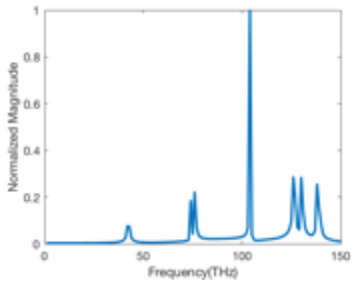

(j) $k_x = \pi/a, k_y = 0.8\pi/a$

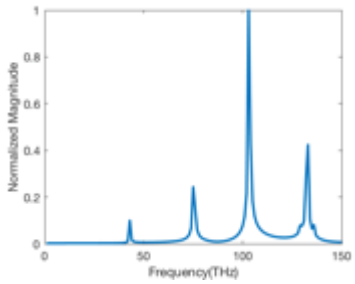

(k) $k_x = k_y = \pi/a$

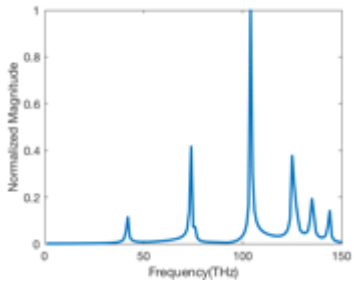

(l) $k_x = k_y = 0.8\pi/a$

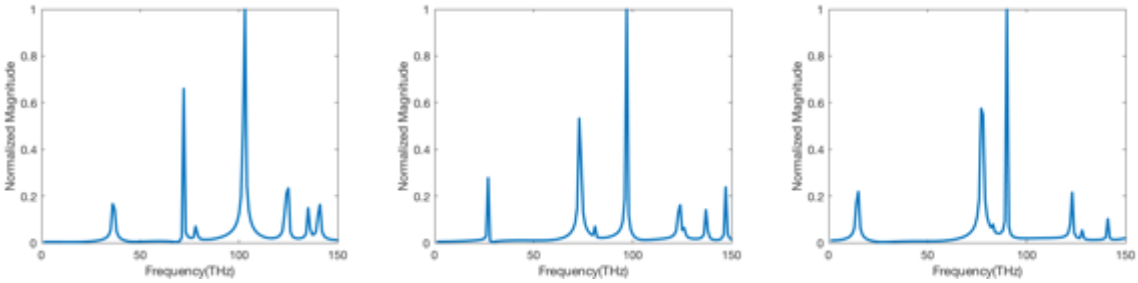

(m) $k_x = k_y = 0.6\pi/a$ (n) $k_x = k_y = 0.4\pi/a$ (o) $k_x = k_y = 0.2\pi/a$

Figure 3.7 Frequency spectra at each wave vector for square lattice

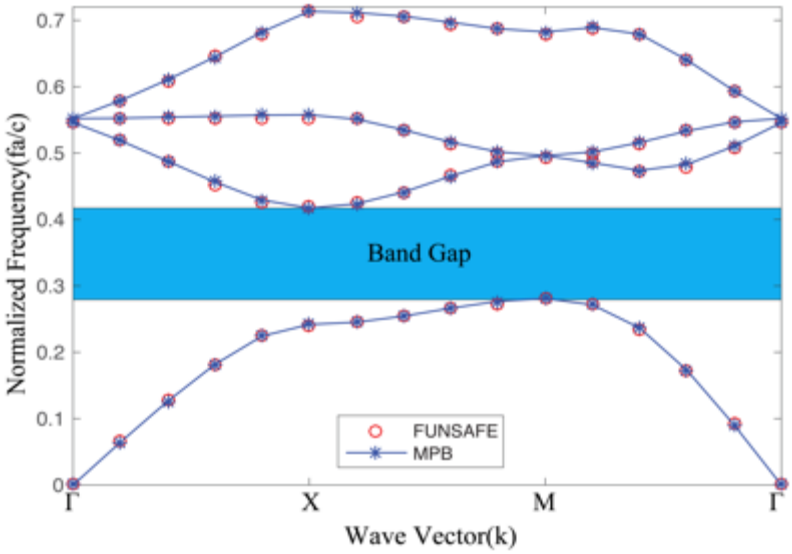

Figure 3.8 Band diagram of square lattice

Triangular Lattice

The second test case is to simulate the light propagation in the $x\sim y$ plane of a triangular array of dielectric columns as shown in Fig 3.2, with lattice constant $a = 200nm$. The proposed photonic crystal consists of silicon$(\varepsilon = 12.0)$ rods in air, with radius $r = 40nm$.

The simulation is run on the unit cell shown in Fig. 3.2(b) over frequency range of 0-150THz in TM mode with 15 different boundary conditions mentioned in last section.

Fourier transform of temporal response of z-component of electric field at 15 different wave vectors $\boldsymbol{k}$ are shown in Fig. 3.9(a-o). The band diagram is shown in Fig. 3.10. The simulation result of band diagram is compared with MPB[78], the results match each other well. As illustrated in Fig. 3.10, the band gap of the proposed photonic crystal is from 410THz to 667THz.

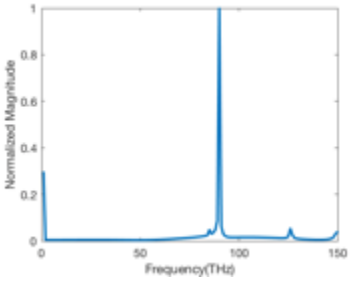

(a) $k_x = 0.0, k_y = 0.0$

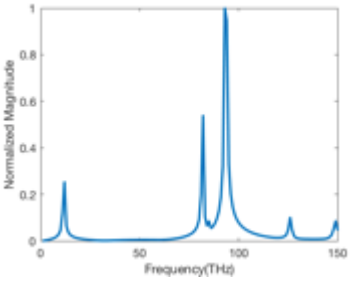

(b) $k_x = 0, k_y = 0.4\pi/\sqrt{3}a$

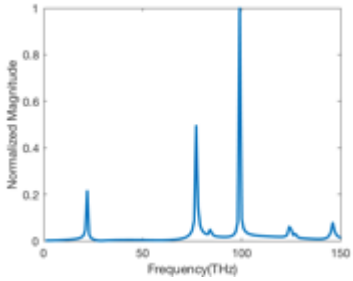

(c) $k_x = 0, k_y = 0.8\pi/\sqrt{3}a$

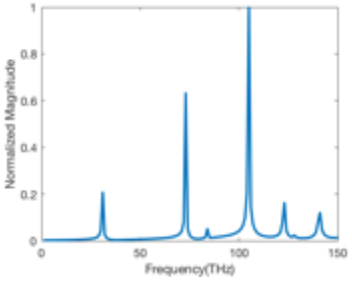

(d) $k_x = 0, k_y = 1.2\pi/\sqrt{3}a$

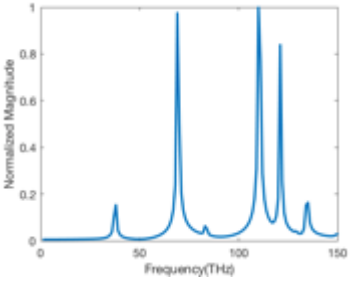

(e) $k_x = 0, k_y = 1.6\pi/\sqrt{3}a$

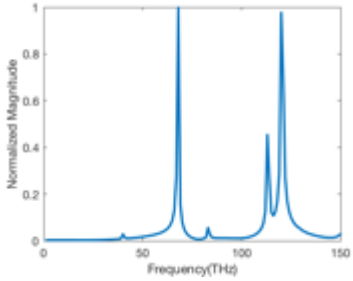

(f) $k_x = 0, k_y = 2\pi/\sqrt{3}a$

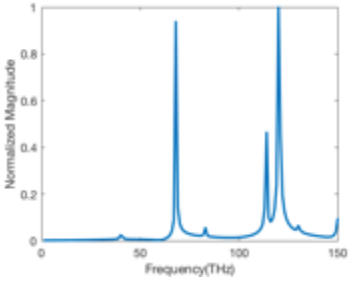

(g) $k_x = 0.4\pi/3a$, $k_y = 2\pi/\sqrt{3}a$

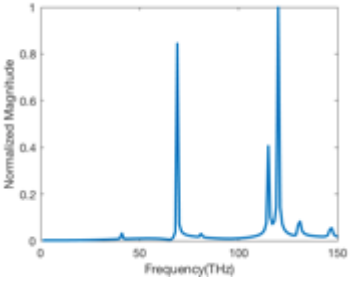

(f) $k_x = 0.8\pi/3a$, $k_y = 2\pi/\sqrt{3}a$

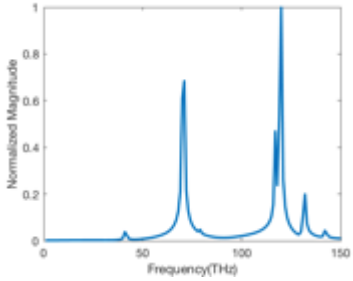

(i) $k_x = 1.2\pi/3a$, $k_y = 2\pi/\sqrt{3}a$

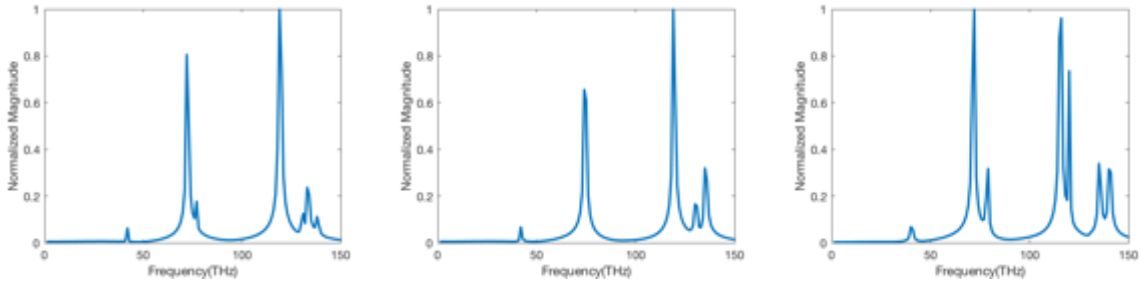

(j) $k_x = 1.6\pi/3a$, $k_y = 2\pi/\sqrt{3}a$ (k) $k_x = 2\pi/3a$, $k_y = 2\pi/\sqrt{3}a$ (l) $k_x = 1.6\pi/3a$, $k_y = 1.6\pi/\sqrt{3}a$

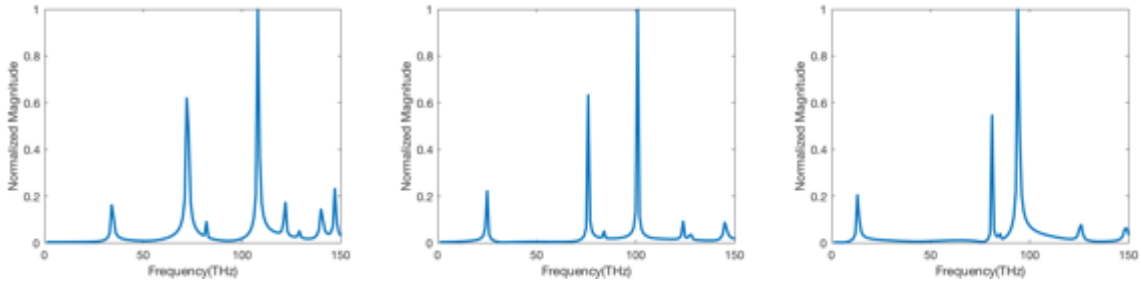

(m) $k_x = 1.2\pi/3a$, $k_y = 1.2\pi/\sqrt{3}a$ (n) $k_x = 0.8\pi/3a$, $k_y = 0.8\pi/\sqrt{3}a$ (o) $k_x = 0.4\pi/3a$, $k_y = 0.4\pi/\sqrt{3}a$

Figure 3.9 Frequency spectra at each wave vector for triangular lattice

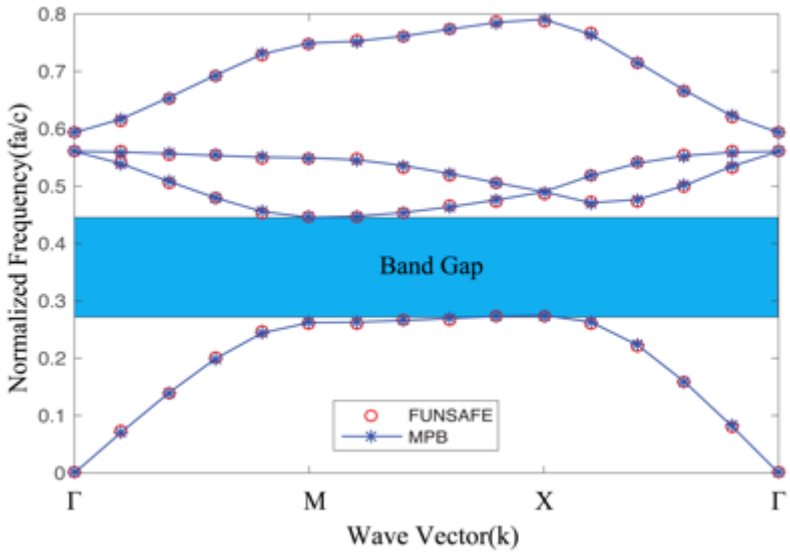

Figure 3.10 Band diagram of triangular lattice

Approach Array Model

The strategy used in exciting the monitoring waves may cause problems such as missing peaks especially when the shape is complex. This will increase the inaccuracy in the design cycle. Also, the magnitude of the peaks at the frequency spectra is random, which can introduce disturbance and leads to unsteadiness in the design cycle. For the reasons above, an approach array model for simulation of the photonic crystals for design purposes is proposed.

Reflection and Transmission

Scattering parameters describe the input-output relationship between ports in an electrical system. Regarding a typical two-port network, the scattering matrix shows the relationship between the outgoing waves b_1, b_2 and incoming waves a_1, a_2 that are incident at the two ports:

$$\begin{bmatrix} b_1 \\ b_2 \end{bmatrix} = \begin{bmatrix} S_{11} & S_{12} \\ S_{21} & S_{22} \end{bmatrix} \begin{bmatrix} a_1 \\ a_2 \end{bmatrix}, S = \begin{bmatrix} S_{11} & S_{12} \\ S_{21} & S_{22} \end{bmatrix} \quad (3.21)$$

The matrix elements, S_{11}, S_{12}, S_{21}, S_{22} are referred to as the scattering parameters. The parameters S_{11} and S_{22} represent reflection coefficients, and parameters S_{21} and S_{12} represent transmission coefficients.

In practice, the most commonly quoted parameter in regards to photonic crystal and metamaterials are transmission and reflection. Equation (3.22) shows the relation between transmission and scattering parameters, and Eq.(3.23) shows the relation between reflection and scattering parameters.

$$Reflection = {S_{11}}^2 \quad (3.22)$$

$$Transmission = {S_{21}}^2 \quad (3.23)$$

To calculate reflection and transmission, electric field and magnetic filed are monitored at the excitation port and collection port. Transmitted, incident and reflected power can be obtained from the monitored field. The formulas to calculate reflection and transmission are expressed as follow:

$$Reflection(k) = S_{11}(k)^2 = \frac{P\_R(k)}{P\_I(k)} \tag{3.24}$$

$$Transmission(k) = S_{21}(k)^2 = \frac{P\_T(k)}{P\_I(k)} \tag{3.25}$$

In Eqs.(3.24-3.25), $P\_T(k)$ represents the transmitted power at frequency k, $P\_I(k)$ represents the incident power at frequency k, and $P\_R(k)$ represents the reflected power at frequency k. The formula to calculate power is expressed in Eq.(3.26), and Eqs.(3.27-3.29) are the FEM implementations of Eq.(3.26).

$$Power = E * \bar{H} \tag{3.26}$$

$$P\_T(k) = \int_{port2} \sum_{ng=1}^{ngauss} weight \cdot Jacobian \cdot E_{fourier}\_T(m,k,ng) \times \overline{H_{fourier}\_T(m,k,ng)} \tag{3.27}$$

$$P\_I(k) = \int_{port1} \sum_{ng=1}^{ngauss} weight \cdot Jacobian \cdot E_{fourier}\_I(m,k,ng) \times \overline{H_{fourier}\_I(m,k,ng)} \tag{3.28}$$

$$P\_R(k) = \int_{port1} \sum_{ng=1}^{ngauss} weight \cdot Jacobian \cdot E_{fourier}\_R(m,k,ng) \times \overline{H_{fourier}\_R(m,k,ng)} \tag{3.29}$$

Square Lattice

The approach array model for square lattice is a 10×1 array as shown in Fig. 3.11. Periodic conditions are applied on the boundary $y = 0$ and $y = a$. A modulated Gaussian pulse is applied at Port 1 to excite the electromagnetic modes over a wide range of frequencies. The temporal responses at Port 1 and Port 2 are recorded at each time step until the solution has converged. Then a Fourier transform of the temporal results is used to obtain the frequency spectra of electric field and magnetic field.

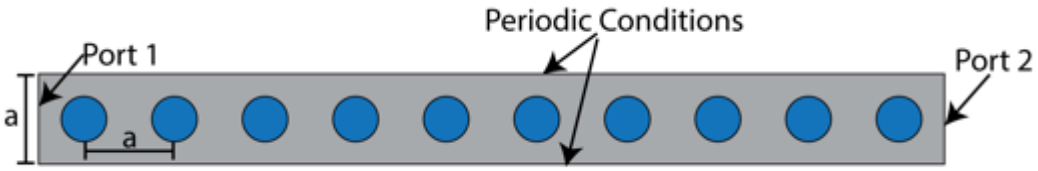

Figure 3.11 Approach array model for square lattice

The reflection of the approach array model for square lattice is shown in Fig. 3.12(a). The comparison of that with the band diagram is illustrated in Fig. 3.12(b). A small mismatch can be observed since the approach model does not have the infinite periodicity along the x-axis as the unit cell model. However, considering its steadiness, it is a good approach for design purpose. The approach array model is used for design cycles to be discussed in Chapter IV, and the final optimized photonic crystals will be simulated with the unit cell model again to get the exact band diagram.

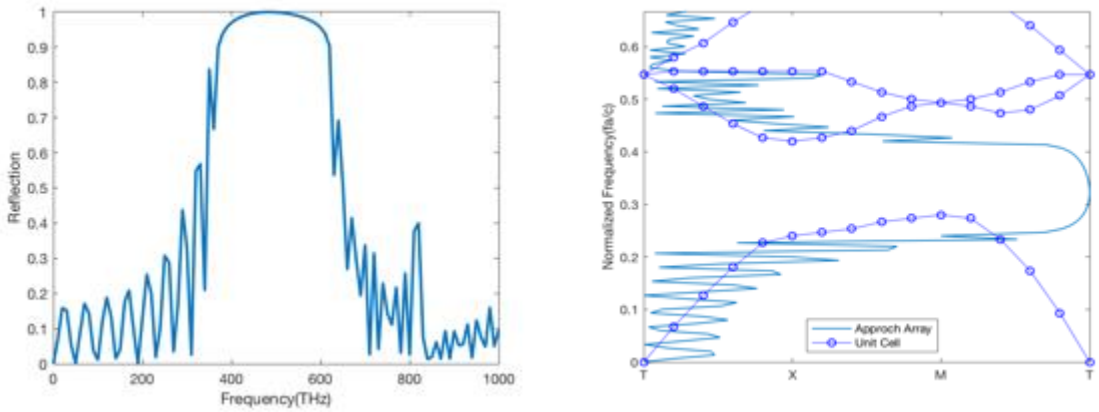

(a) Reflection (b)Reflection and band diagram

Figure 3.12 Results of approach array model for square lattice

CHAPTER IV

SENSITIVITY ANALYSIS AND SHAPE OPTIMIZATION OF PHOTONIC CRYSTALS

Cost Function and Sensitivity Analysis

The target of shape optimization of photonic crystals is to realize band gap shift. For the target, a generalized cost function is proposed as follow:

$$costI = \sum_{k=f1}^{f2} Transmission(k) + \sum_{k=f3}^{f4} Reflection(k) \tag{4.1}$$

The cost function ensures minimization of transmission at frequency range $f1 - f2$ and minimization of reflection at frequency range of $f3 - f4$. When $costI$ is minimized, the band gap of the designed photonic crystal will shift to the desired range of $f1 - f2$. The frequency range of $f3 - f4$ here is to ensure that the designed photonic crystal only have band gap at the desired frequency range.

From the definition in Eqs.(3.24-3.25), the cost function can be expressed as:

$$costI = \sum_{k=f1}^{f2} \frac{P\_T(k)}{P\_I(k)} + \sum_{k=f3}^{f4} \frac{P\_R(k)}{P\_I(k)} \tag{4.2}$$

where $P\_T(k)$,$P\_I(k)$ and $P\_R(k)$ represent the transmitted, incident and reflected power at frequency k,respectively, and the FEM formulation is shown in Eqs. (3.27-3.29). The Fourier transform terms of electric and magnetic field in Eq. (3.27) can be expressed as:

$$E_{fourier}\_T(m,k,ng) = \sum_{i=1}^{ncyc} E\_T(i,m,ng) \cdot e^{-j\omega(k)i\Delta t}\Delta t \tag{4.3}$$

$$\overline{H_{fourier}\_T(m,k,ng)} = \sum_{i=1}^{ncyc} H\_T(i,m,ng) \cdot e^{j\omega(k)i\Delta t}\Delta t \tag{4.4}$$

By defining $\phi(i,k) = e^{-j\omega(k)i\Delta t}\Delta t$, Eqs.(4.3-4.4) are rewritten as:

$$E_{fourier}\_T(m,k,ng) = \sum_{i=1}^{ncyc} E\_T(i,m,ng)\cdot\phi(i,k) \tag{4.5}$$

$$\overline{H_{fourier}\_T(m,k,ng)} = \sum_{i=1}^{ncyc} H\_T(i,m,ng)\cdot\overline{\phi(i,k)} \tag{4.6}$$

Similarly, for the Fourier transform terms of electric and magnetic field in Eqs.(3.28-3.29), we have:

$$E_{fourier}\_I(m,k,ng) = \sum_{i=1}^{ncyc} E\_I(i,m,ng)\cdot\phi(i,k) \tag{4.7}$$

$$\overline{H_{fourier}\_I(m,k,ng)} = \sum_{i=1}^{ncyc} H\_I(i,m,ng)\cdot\overline{\phi(i,k)} \tag{4.8}$$

$$E_{fourier}\_R(m,k,ng) = \sum_{i=1}^{ncyc} E\_R(i,m,ng)\cdot\phi(i,k) \tag{4.9}$$

$$\overline{H_{fourier}\_R(m,k,ng)} = \sum_{i=1}^{ncyc} H\_R(i,m,ng)\cdot\overline{\phi(i,k)} \tag{4.10}$$

Then the Eqs(3.27-3.29) can be expressed as follow:

$$P\_T(k) = \int_{port2}\sum_{ng=1}^{ngauss} w\cdot J\cdot\sum_{i=1}^{ncyc} E\_T(i,m,ng)\cdot\phi(i,k)\times\sum_{i=1}^{ncyc} H\_T(i,m,ng)\cdot\overline{\phi(i,k)} \tag{4.11}$$

$$P\_I(k) = \int_{port1}\sum_{ng=1}^{ngauss} w\cdot J\cdot\sum_{i=1}^{ncyc} E\_I(i,m,ng)\cdot\phi(i,k)\times\sum_{i=1}^{ncyc} H\_I(i,m,ng)\cdot\overline{\phi(i,k)} \tag{4.12}$$

$$P\_R(k) = \int_{port1}\sum_{ng=1}^{ngauss} w\cdot J\cdot\sum_{i=1}^{ncyc} E\_R(i,m,ng)\cdot\phi(i,k)\times\sum_{i=1}^{ncyc} H\_R(i,m,ng)\cdot\overline{\phi(i,k)} \tag{4.13}$$

The sensitivities of the cost function for both forward sensitivity and adjoint formulation are discussed in details in the following sections.

Forward Sensitivity

The general method of calculating total differential of cost function with respect to the design variable β with forward sensitivity analysis was discussed in Chapter II. For the design problem proposed in this dissertation, it becomes more complicated since the cost function is related to the Fourier transform of the temporal results. For the proposed cost function, the first and second terms of Eq.(2.42) are zero, only the third term is

considered. The total differential of cost function with respect to the design variable β is expressed as:

$$\begin{aligned}\frac{dcostI}{d\beta} &= \sum_{k=f1}^{f2}\frac{dTransmission(k)}{d\beta}+\sum_{k=f3}^{f4}\frac{dReflection(k)}{d\beta}\\ &=\sum_{k=f1}^{f2}\left(\frac{\partial Transmission(k)}{\partial P\_T(k)}\cdot\frac{\partial P\_T(k)}{\partial\beta}+\frac{\partial Transmission(k)}{\partial P\_I(k)}\cdot\frac{\partial P\_I(k)}{\partial\beta}\right)\\ &\quad+\sum_{k=f1}^{f2}\left(\frac{\partial Reflection(k)}{\partial P\_R(k)}\cdot\frac{\partial P\_R(k)}{\partial\beta}+\frac{\partial Reflection(k)}{\partial P\_I(k)}\cdot\frac{\partial P\_I(k)}{\partial\beta}\right)\end{aligned} \tag{4.14}$$

The sensitivities of the power terms in Eq.(4.14) can be expressed as :

$$\begin{aligned}\frac{\partial P\_T(k)}{\partial\beta} &= \int_{port2}\sum_{ng=1}^{ngauss} wJ\left(\sum_{i=1}^{ncyc}\frac{\partial E\_T(i,m,ng)}{\partial\beta}\cdot\phi(i,k)\times\sum_{i=1}^{ncyc}H\_T(i,m,ng)\cdot\overline{\phi(\iota,k)}\right)\\ &\quad+\int_{port2}\sum_{ng=1}^{ngauss} wJ\left(\sum_{i=1}^{ncyc}\frac{\partial H\_T(i,m,ng)}{\partial\beta}\cdot\overline{\phi(\iota,k)}\times\sum_{i=1}^{ncyc}E\_T(i,m,ng)\cdot\phi(i,k)\right)\end{aligned} \tag{4.15}$$

$$\begin{aligned}\frac{\partial P\_I(k)}{\partial\beta} &= \int_{port1}\sum_{ng=1}^{ngauss} wJ\left(\sum_{i=1}^{ncyc}\frac{\partial E\_I(i,m,ng)}{\partial\beta}\cdot\phi(i,k)\times\sum_{i=1}^{ncyc}H\_I(i,m,ng)\cdot\overline{\phi(\iota,k)}\right)\\ &\quad+\int_{port1}\sum_{ng=1}^{ngauss} wJ\left(\sum_{i=1}^{ncyc}\frac{\partial H\_I(i,m,ng)}{\partial\beta}\cdot\overline{\phi(\iota,k)}\times\sum_{i=1}^{ncyc}E\_I(i,m,ng)\cdot\phi(i,k)\right)\end{aligned} \tag{4.16}$$

$$\begin{aligned}\frac{\partial P\_R(k)}{\partial\beta} &= \int_{port1}\sum_{ng=1}^{ngauss} wJ\left(\sum_{i=1}^{ncyc}\frac{\partial E\_R(i,m,ng)}{\partial\beta}\cdot\phi(i,k)\times\sum_{i=1}^{ncyc}H\_R(i,m,ng)\cdot\overline{\phi(\iota,k)}\right)\\ &\quad+\int_{port1}\sum_{ng=1}^{ngauss} wJ\left(\sum_{i=1}^{ncyc}\frac{\partial H\_R(i,m,ng)}{\partial\beta}\cdot\overline{\phi(\iota,k)}\times\sum_{i=1}^{ncyc}E\_R(i,m,ng)\cdot\phi(i,k)\right)\end{aligned} \tag{4.17}$$

In Eqs.(4.15-4.17), the sensitivities of electric and magnetic field are obtained by solving linear equations:

$$\frac{\partial q^i}{\partial\beta}=-\left[\frac{\partial R^i}{\partial q^i}\right]^{-1}\left(\frac{\partial R^i}{\partial X}\frac{\partial X}{\partial\beta}+\frac{\partial R^i}{\partial q^{i-1}}\frac{\partial q^{i-1}}{\partial\beta}+\frac{\partial R^i}{\partial q^{i-2}}\frac{\partial q^{i-2}}{\partial\beta}\right) \tag{4.18}$$

For each design variable, one linear equation needs to be solved at each time step. The computational costs for the forward mode sensitivities scale with the number of design variables.

Discrete Adjoint Formulation

To overcome the disadvantages of forward mode sensitivities, discrete adjoint formulation is proposed. The general method of calculating total differential of cost function with respect to the design variable β with discrete adjoint formulation was discussed in Chapter II. In Eq.(2.42), $\frac{dcostI}{dQ}$ is the term to be derived, the total differential of cost function with respect to solution Q is expressed as:

$$\begin{aligned}\frac{dcostI}{dQ} &= \sum_{k=f1}^{f2} \frac{dTransmission(k)}{dQ} + \sum_{k=f3}^{f4} \frac{dReflection(k)}{dQ} \\ &= \sum_{k=f1}^{f2} \left(\frac{\partial Transmission(k)}{\partial P\_T(k)} \cdot \frac{\partial P\_T(k)}{\partial Q} + \frac{\partial Transmission(k)}{\partial P\_I(k)} \cdot \frac{\partial P\_I(k)}{\partial Q} \right) \\ &\quad + \sum_{k=f1}^{f2} \left(\frac{\partial Reflection(k)}{\partial P\_R(k)} \cdot \frac{\partial P\_R(k)}{\partial Q} + \frac{\partial Reflection(k)}{\partial P\_I(k)} \cdot \frac{\partial P\_I(k)}{\partial Q} \right)\end{aligned} \tag{4.19}$$

The sensitivities of the power term is Eq.(4.19) can be expressed as :

$$\begin{aligned}\frac{\partial P\_T(k)}{\partial Q} &= \int_{port2} \sum_{ng=1}^{ngauss} wJ \left(\sum_{i=1}^{ncyc} \frac{\partial E\_T(i,m,ng)}{\partial Q} \cdot \phi(i,k) \times \sum_{i=1}^{ncyc} H\_T(i,m,ng) \cdot \overline{\phi(\iota,k)} \right) \\ &\quad + \int_{port2} \sum_{ng=1}^{ngauss} wJ \left(\sum_{i=1}^{ncyc} \frac{\partial H\_T(i,m,ng)}{\partial Q} \cdot \overline{\phi(\iota,k)} \times \sum_{i=1}^{ncyc} E\_T(i,m,ng) \cdot \phi(i,k) \right)\end{aligned} \tag{4.20}$$

Equation (4.20) can be rewritten as:

$$\begin{aligned}\frac{\partial P\_T(k)}{\partial Q} &= \int_{port2} \sum_{ng=1}^{ngauss} wJ \left(\overline{H_{fourier}\_T(m,k,ng)} \times \sum_{i=1}^{ncyc} \frac{\partial E\_T(i,m,ng)}{\partial Q} \cdot \phi(i,k) \right) \\ &\quad + \int_{port2} \sum_{ng=1}^{ngauss} wJ \left(E_{fourier}\_T(m,k,ng) \times \sum_{i=1}^{ncyc} \frac{\partial H\_T(i,m,ng)}{\partial Q} \cdot \overline{\phi(\iota,k)} \right)\end{aligned} \tag{4.21}$$

Since the terms $\frac{\partial E\_T(i,m,ng)}{\partial Q}$ and $\frac{\partial H\_T(i,m,ng)}{\partial Q}$ does not depend on the time step i, Eq.(4.21) can be rewritten as:

$$\frac{\partial P\_T(k)}{\partial Q} = \frac{\partial P\_T1(k)}{\partial Q} \sum_{i=1}^{ncyc} \phi(i,k) + \frac{\partial P\_T2(k)}{\partial Q} \sum_{i=1}^{ncyc} \overline{\phi(\iota,k)} \tag{4.22}$$

where

$$\frac{\partial P\_T1(k)}{\partial Q} = \int_{port2} \sum_{ng=1}^{ngauss} wJ \left(\overline{H_{fourier}\_T(m,k,ng)} \times \frac{\partial E\_T(m,ng)}{\partial Q} \right) \tag{4.23}$$

$$\frac{\partial P\_T2(k)}{\partial Q} = \int_{port2} \sum_{ng=1}^{ngauss} wJ \left(E_{fourier}\_T(m,k,ng) \times \frac{\partial H\_T(m,ng)}{\partial Q} \right) \tag{4.24}$$

Similarly, we have:

$$\frac{\partial P\_I(k)}{\partial Q} = \frac{\partial P\_I1(k)}{\partial Q} \sum_{i=1}^{ncyc} \phi(i,k) + \frac{\partial P\_I2(k)}{\partial Q} \sum_{i=1}^{ncyc} \overline{\phi(\iota,k)} \tag{4.25}$$

$$\frac{\partial P\_R(k)}{\partial Q} = \frac{\partial P\_R1(k)}{\partial Q} \sum_{i=1}^{ncyc} \phi(i,k) + \frac{\partial P\_R2(k)}{\partial Q} \sum_{i=1}^{ncyc} \overline{\phi(\iota,k)} \tag{4.26}$$

where

$$\frac{\partial P\_I1(k)}{\partial Q} = \int_{port2} \sum_{ng=1}^{ngauss} wJ \left(\overline{H_{fourier}\_I(m,k,ng)} \times \frac{\partial E\_I(m,ng)}{\partial Q} \right) \tag{4.27}$$

$$\frac{\partial P\_I2(k)}{\partial Q} = \int_{port2} \sum_{ng=1}^{ngauss} wJ \left(E_{fourier}\_I(m,k,ng) \times \frac{\partial H\_I(m,ng)}{\partial Q} \right) \tag{4.28}$$

$$\frac{\partial P\_R1(k)}{\partial Q} = \int_{port2} \sum_{ng=1}^{ngauss} wJ \left(\overline{H_{fourier}\_R(m,k,ng)} \times \frac{\partial E\_R(m,ng)}{\partial Q} \right) \tag{4.29}$$

$$\frac{\partial P\_R2(k)}{\partial Q} = \int_{port2} \sum_{ng=1}^{ngauss} wJ \left(E_{fourier}\_R(m,k,ng) \times \frac{\partial H\_R(m,ng)}{\partial Q} \right) \tag{4.30}$$

Finally, the total differential of cost function with respect to solution Q is expressed as:

$$\begin{aligned} \frac{dcostI}{dQ} = & \sum_{i=1}^{ncyc} \sum_{k=f1}^{f2} \left(\frac{\partial S21(k)}{\partial P\_T(k)} \cdot \frac{\partial P\_T1(k)}{\partial Q} + \frac{\partial S21(k)}{\partial P\_I(k)} \cdot \frac{\partial P\_I1(k)}{\partial Q} \right) \phi(i,k) \\ & + \sum_{i=1}^{ncyc} \sum_{k=f1}^{f2} \left(\frac{\partial S21(k)}{\partial P\_T(k)} \cdot \frac{\partial P\_T2(k)}{\partial Q} + \frac{\partial S21(k)}{\partial P\_I(k)} \cdot \frac{\partial P\_I2(k)}{\partial Q} \right) \overline{\phi(\iota,k)} \\ & + \sum_{i=1}^{ncyc} \sum_{k=f3}^{f4} \left(\frac{\partial S11(k)}{\partial P\_R(k)} \cdot \frac{\partial P\_R1(k)}{\partial Q} + \frac{\partial S11(k)}{\partial P\_I(k)} \cdot \frac{\partial P\_I1(k)}{\partial Q} \right) \overline{\phi(\iota,k)} \\ & + \sum_{i=1}^{ncyc} \sum_{k=f3}^{f4} \left(\frac{\partial S11(k)}{\partial P\_R(k)} \cdot \frac{\partial P\_R2(k)}{\partial Q} + \frac{\partial S11(k)}{\partial P\_I(k)} \cdot \frac{\partial P\_I2(k)}{\partial Q} \right) \overline{\phi(\iota,k)} \end{aligned} \tag{4.31}$$

The computational costs for the discrete adjoint formulation do not scale with the number of design variables.

Verification of Shape Sensitivity Derivatives

For the photonic crystal with square lattice proposed in Chapter III, the time accurate sensitivity derivatives are computed with three methods to verify the correctness of implementation; they are: finite difference method, forward sensitivity method and adjoint formulation. For this case, the design variable β is the radius of the circle r. For better clarification, as shown in Fig. 4.1, $\frac{dReflection(k)}{d\beta}$ are plotted at each frequency point for comparison of finite difference and forward sensitivity. For adjoint method, the matrix to be solved is determined by the number of cost functions. For forward sensitivity, the matrix to be solved is determined by the number of design variables. That's why Fig. 4.1 does not show the plot of $\frac{dReflection(k)}{d\beta}$ of adjoint method for each frequency point.

To make further verification, now let the cost function be as follow:

$$costI = \sum_{k=f1}^{f2} Reflection(k) \tag{4.32}$$

where $f1 = 200THz\ and\ f2 = 600T$. Table 4.1 shows the comparison of $\frac{dcostI}{d\beta}$ generated from the finite different approach, the forward sensitivity approach and the discrete adjoint approach.

Table 4.1 Comparison of Sensitivity Derivatives

Approach	$\frac{dcostI}{d\beta}$
Finite Difference	-0.962499999968E+02
Forward Sensitivity	-0.9626056573E+02
Discrete Adjoint	-0.9626056587E+02

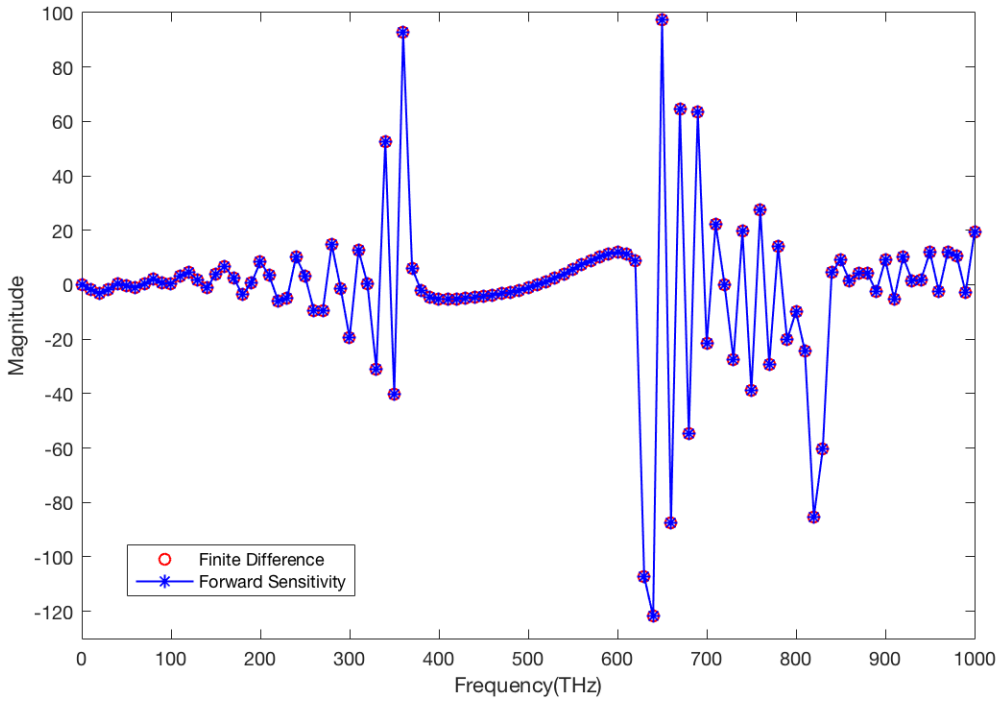

Figure 4.1 Comparison of sensitivity at each frequency for square lattice

Optimization Results and Application on Optical waveguide

Photonic Crystal Waveguide

The well-known metallic pipe waveguide provides lossless transmission, but it only works for microwaves. To provide lossless transmission for infrared and visible light, dielectric guides were developed. The dielectric waveguide relies on total internal reflection to ensure lossless transmission. However, if it curves tightly, the angle of incidence is too large for total internal reflection to occur, as a result, light is lost at the corners.

By applying the technique of photonic crystal into waveguides, lossless transmission even at sharp corners can be obtained. Considering the band gap of photonic

crystals discussed earlier, light within the gap is forbidden to transmit through the photonic crystal. By carving a waveguide out of the photonic crystal, light with frequencies in the gap of the photonic crystal can be directed along the waveguide.

By carving different paths out of the photonic crystal with square lattice proposed in Chapter III, waveguides with different transmission directions are obtained. The electric field patterns at 500THz, which is located within the band gap as shown in Fig. 3.8, are shown in Fig.4.2. Fig. 4.2(a) shows electric field pattern within a straight waveguide, Fig. 4.2(b-c) show electric field patterns within 90 degree and 135 degree bent waveguides, and Fig. 4.2(d) shows a U-shaped waveguide.

By optimizing the band gap of photonic crystal, we can obtain optical waveguides at any frequency range desired. In this work, Bezier curves are applied on shape optimization of photonic crystals. The target is to design a dual-band and a triple-band optical waveguide for applications on telecommunication.

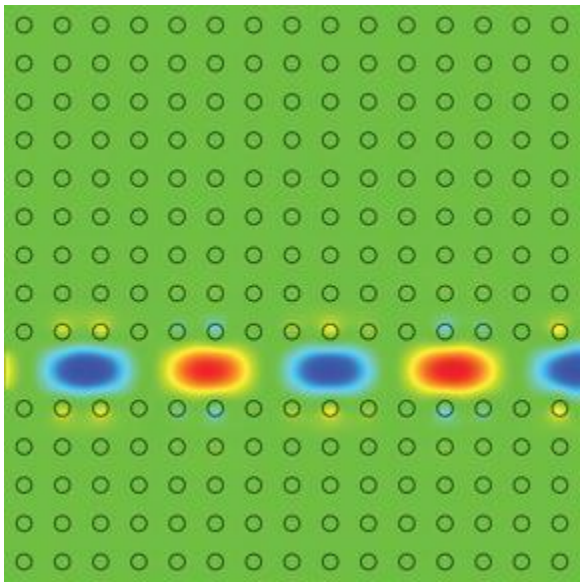

(a) Straight waveguide

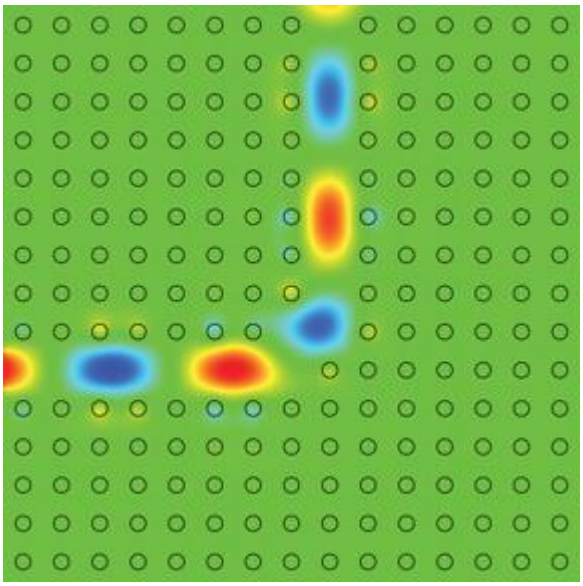

(b) 90 degree bended waveguide

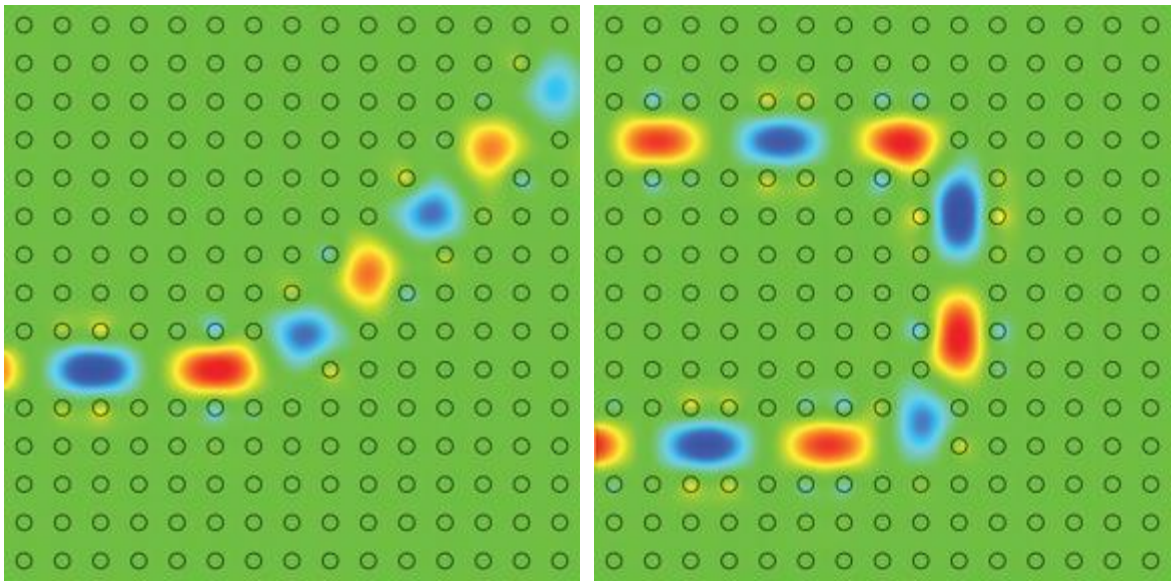

(c) 135 degree bended waveguide (d) U-turn waveguide

Figure 4.2 Electric field pattern in photonic crystal waveguide for frequency f=500THz

Design of Dual-band Waveguide

The base design case is the square lattice made of circles. Consider that the origin point of circle is (0,0) and radius of circle is r. In this design, the circle is divided to two curve segments, the first and last control points of the first curve are the $(r, 0)$ and $(-r, 0)$, and the first and last control points of the second curve are the $(-r, 0)$ and $(r, 0)$. The design variables control the radius of the control points with 10 uniformly distributed angles between the start point and end point. There are 20 design variables in total for the circle with two curve segments.

Since the target is to design dual-band waveguide, the cost function can be expressed as:

$$costI = \sum_{k=f1}^{f2}(1.0 - Reflection(k)) + \sum_{k=f3}^{f4}(1.0 - Reflection(k)) \quad (4.33)$$

where $f_1 = 350THz, f_2 = 450THz, f_3 = 650THz,$ and $f_4 = 750THz$. The shape of optimized unit cell with 20 design variables is shown in Fig.4.3.

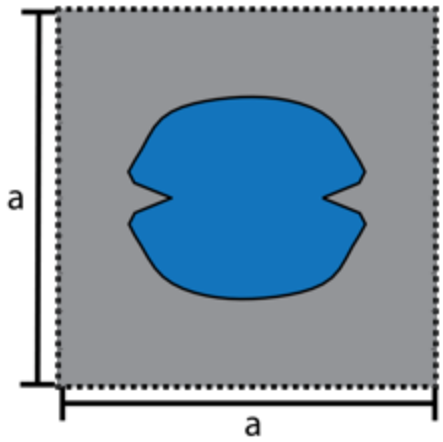

Figure 4.3 Shape of optimized unit cell for dual-band optical waveguide

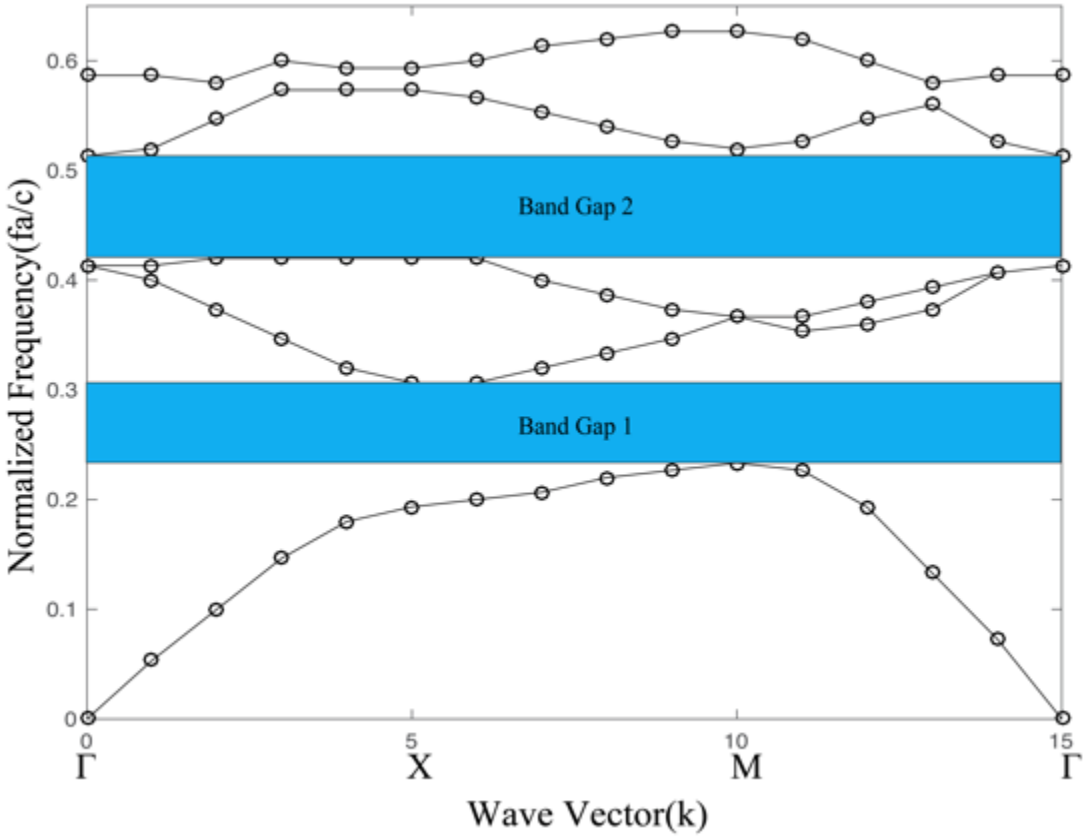

Figure 4.4 Band diagram of optimized photonic crystals for dual-band waveguide

The band diagram is plotted in Fig. 4.4. As is shown, the optimized photonic crystal has band gap at both 352THz~450THz and 630THz~765THz. By carving a path at the designed photonic crystal, a dual-band waveguide is obtained. The electric field patterns of the designed waveguide at 420THz and 680THz are shown in Fig. 4.5.

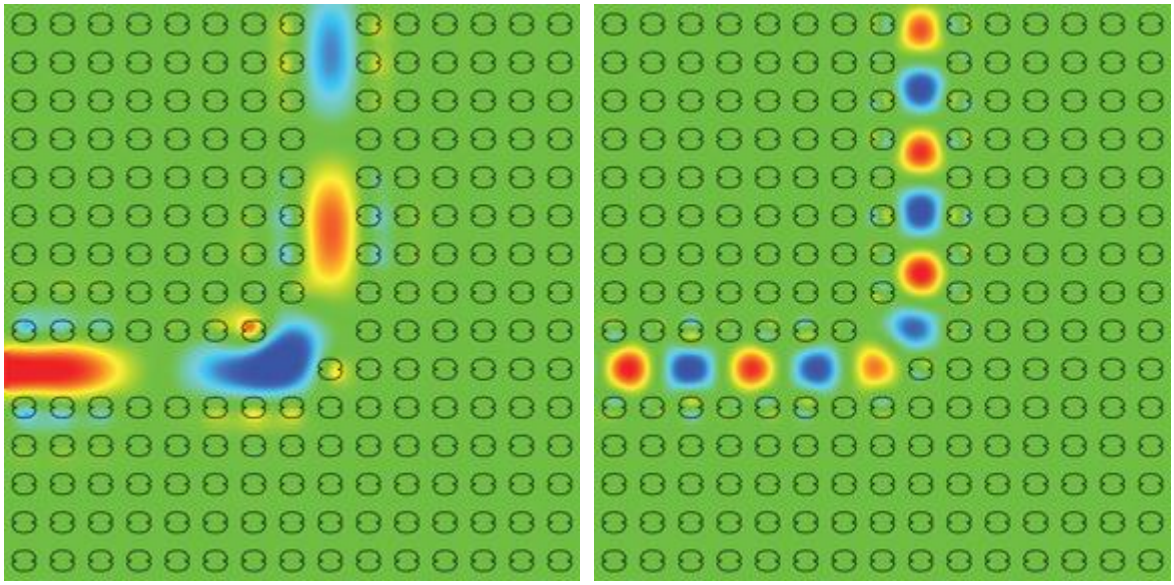

(a) 420THz (b) 680THz

Figure 4.5 Electric field pattern in designed dual-band waveguide

Design of Triple-band Waveguide

In this design, the circle is divided to three curve segments, the first and last control points of the first curve are the $(r, 0)$and $\left(-\frac{1}{2}r, \frac{\sqrt{3}}{2}r\right)$, the first and last control points of the second curve are the $\left(-\frac{1}{2}r, \frac{\sqrt{3}}{2}r\right)$ and $\left(-\frac{1}{2}r, -\frac{\sqrt{3}}{2}r\right)$, and the first and last control points of the third curve are the $\left(-\frac{1}{2}r, -\frac{\sqrt{3}}{2}r\right)$ and $(r, 0)$. The design variables control the radius of the control points with 10 uniformly distributed angles between the start point and end point. Since the three curve segments share the same design variables, the resulted shape is rotationally symmetrical.

Since the target is to design triple-band waveguide, the cost function can be expressed as:

$$costI = \sum_{k=f1}^{f2}(1.0 - Reflection(k)) + \sum_{k=f3}^{f4}(1.0 - Reflection(k)) + \sum_{k=f5}^{f6}(1.0 - Reflection(k)) \quad (4.34)$$

where $f_1 = 300THz, f_2 = 400THz, f_3 = 550THz, f_4 = 650THz, f_5 = 850THz,$ and $f_6 = 950THz$. The shape of optimized unit cell with 10 design variables is shown in Fig. 4.6. The band diagram is plotted in Fig. 4.7. As is shown, the optimized photonic crystal has band gap at 331THz~402THz, 573THz~702THz and 840THz~950THz. The electric field patterns of the designed waveguide at 390THz, 640THz and 880THz are shown in Fig. 4.8.

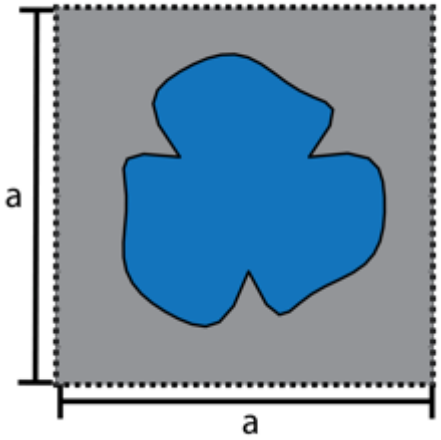

Figure 4.6 Shape of optimized unit cell for triple-band waveguide

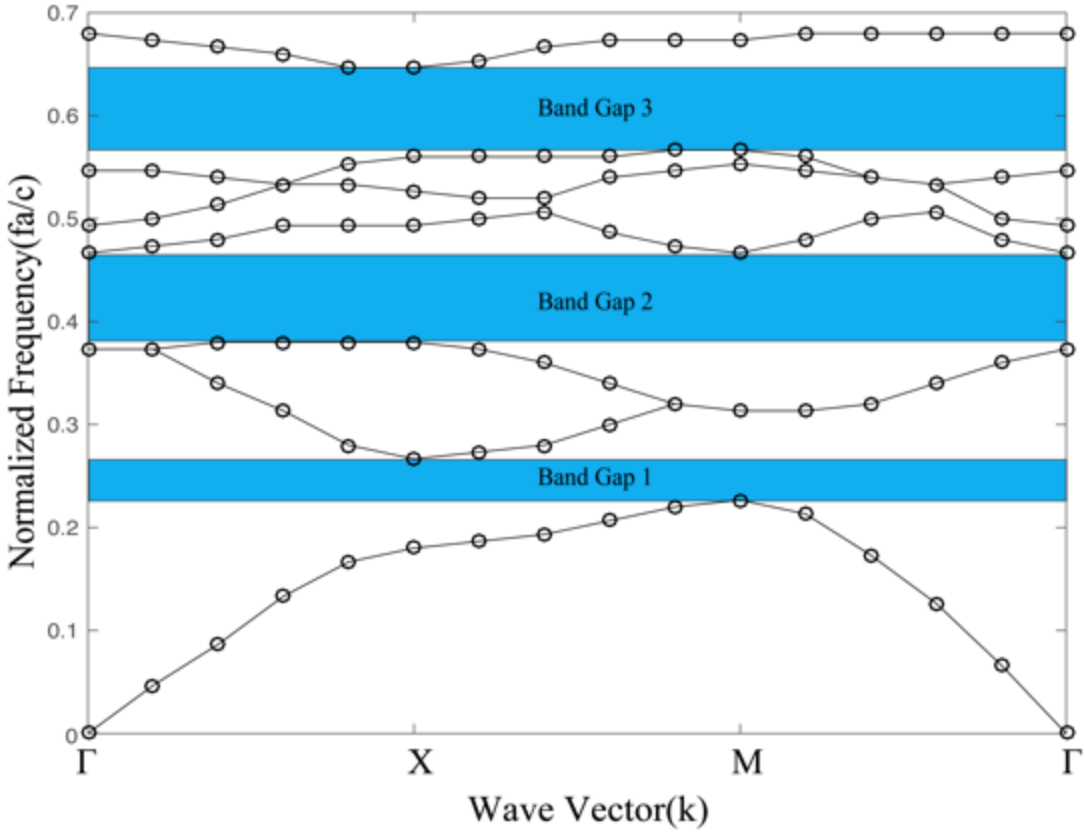

Figure 4.7 Band diagram of optimized photonic crystal for triple-band waveguide

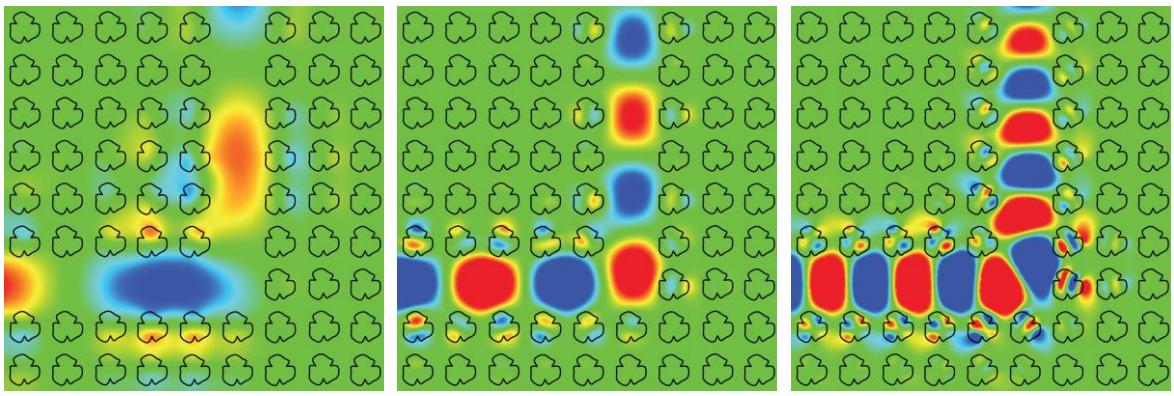

(a) 390THz (b) 640THz (c) 880THz

Figure 4.8 Electric field pattern in designed triple-band waveguide

The optimized waveguides can be applied in telecommunication to the meet the requirement of lossless transmission with any transmitting direction at the desired frequency range.

CHAPTER V

SIMULATION AND OPTIMIZATION OF METAMATERIAL

All-dielectric Metamaterial and Optimization

Proposed Design Model

All-dielectric metamaterials offer a potential low-loss alternative to plasmonic metamaterials at optical frequencies. In the current work, an all-dielectric metamaterial made of silicon on SiO_2 substrate is proposed as the initial design model. Figures 5.1(a-b) illustrate the schematic of metamaterial unit cell and array. The silicon resonators with dimension of $W = 200nm$ and $H = 100nm$ are placed on top of a SiO_2 substrate (regarded infinite) with periodicity of $P = 300nm$. As shown the Fig.5.1(a), the metamaterial is illuminated with polarized light. The electric field is polarized along the x-direction and the magnetic field along the y-direction with wave vector k in z-direction. In this case, the light transmits from the air to the SiO_2 through the silicon resonators.

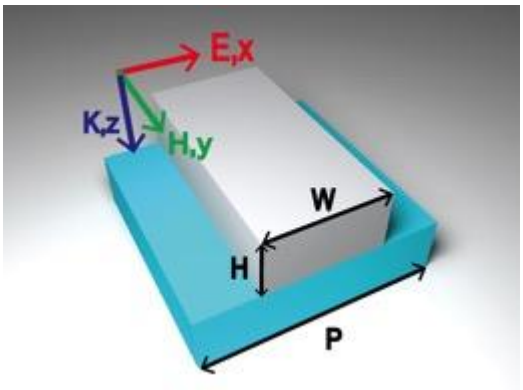

(a)Metamaterial unit cell

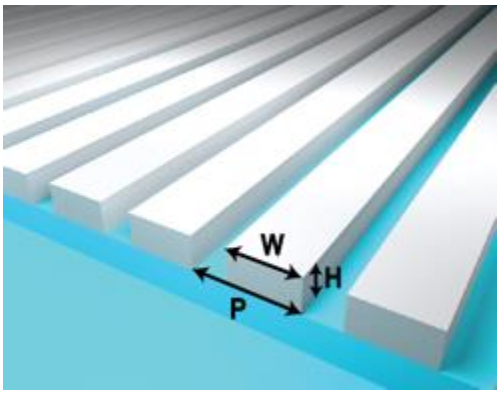

(b) Metamaterial array

Figure 5.1 Proposed initial metamaterial model

Results and Accuracy

The results of reflection over frequency range of 350-650THz are shown in Fig. 5.2(a), with full width at half maximum (FWHM) of 111THz (479~590THz) in reflection. For comparative purposes, the current results are shown with those from the commercial software ANSYS© HFSS[51]. The reflection indicates that the metamaterial has the maximum reflection at 516THz. The electric field distribution at 516THz, depicted in Fig. 5.2(b), clearly illustrates this reflection.

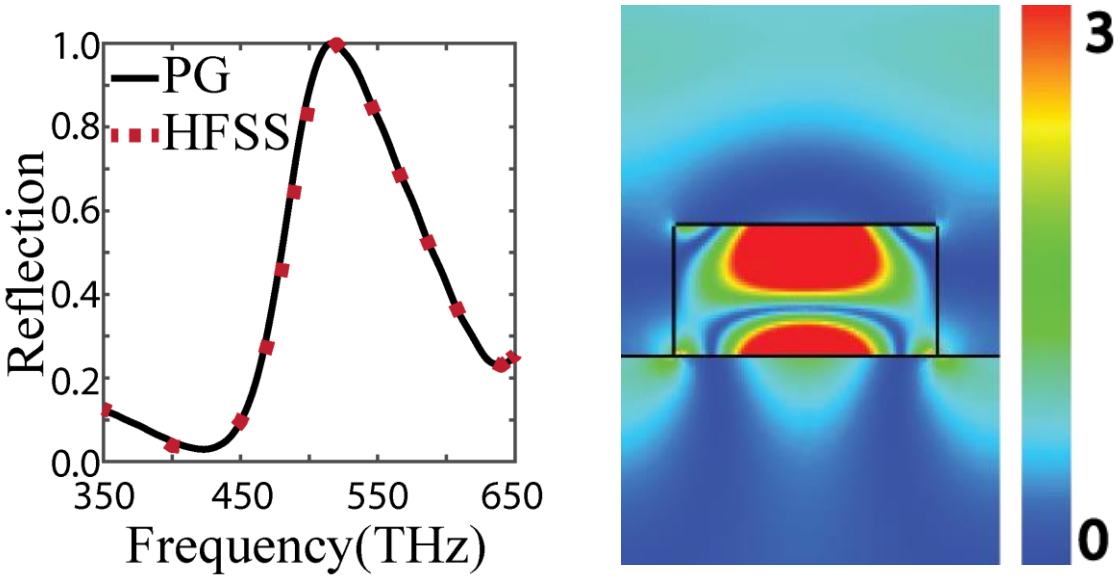

(a) Reflection (b) Electric Field at 516THz

Figure 5.2 Simulation results of initial model

Optimization of All-dielectric Metamaterial

The objective of the current design optimization is to widen the bandwidth of the metamaterial. Accordingly, an objective function is proposed as:

$$I = \int_{f1}^{f2} (1 - Reflection)^2 \, df \tag{5.1}$$

where f_1 and f_2 represent the lower and upper bound of the desired frequency range.

Utilizing the objective function given in Eq.(5.1), with $f_1 = 300THz$ and $f_2 = 700THz$, the optimization was performed using different numbers of design variables. Increasing the number of design variables allows for greater geometric flexibility. Figure 5.3 illustrates the optimization results with 1, 3, and 9 design variables. As seen in Fig. 5.4(a), at 426THz no reflection can be observed from the electric field distribution for the initial model, while high reflection can be observed for the optimized geometries in Figs. 5.4(b)-(d) using different number of design variables.

As shown in Fig. 5.3, the FWHM of reflection for the all-dielectric metamaterial increases from 111THz to 277THz, 285THz, and 303THz with 1, 3, and 9 design variables, respectively. For the optimized result with 9 design variables, the FWHM of reflection ranges from 376 to 679THz. As shown in Fig. 5.5, the electric field distributions at 404THz, 505THz and 620THz are simulated to demonstrate the high reflection property of the optimized metamaterial over the wide frequency range.

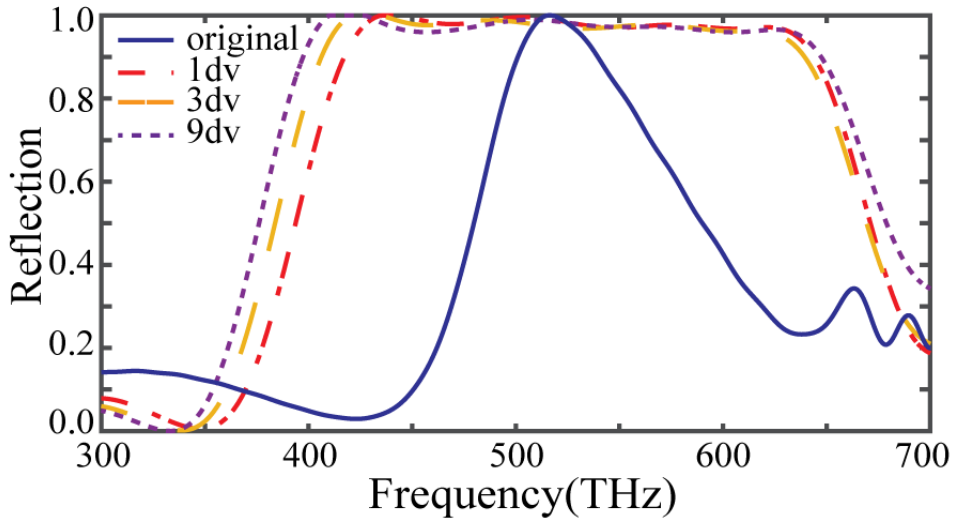

Figure 5.3 Comparison of reflection over 300-700THz

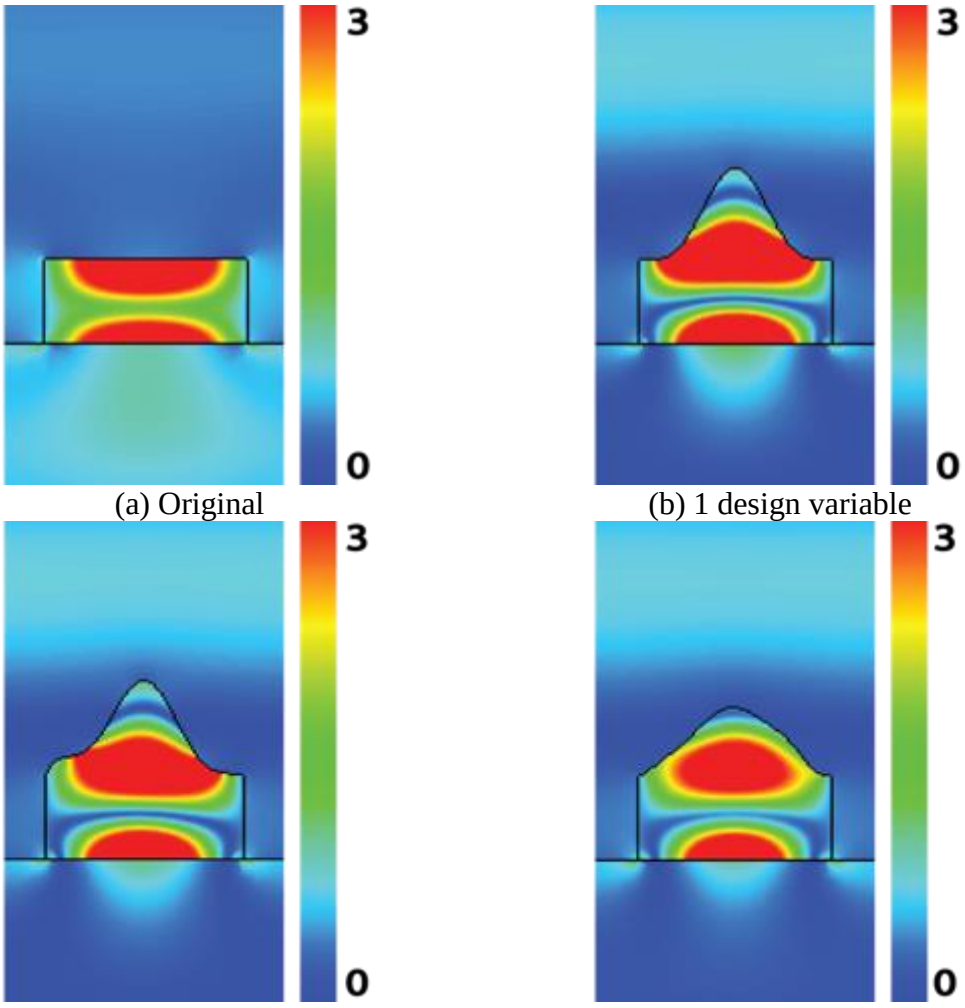

(a) Original (b) 1 design variable

(c) 3 design variables (d) 9 design variables

Figure 5.4 Electric field distribution at 426THz

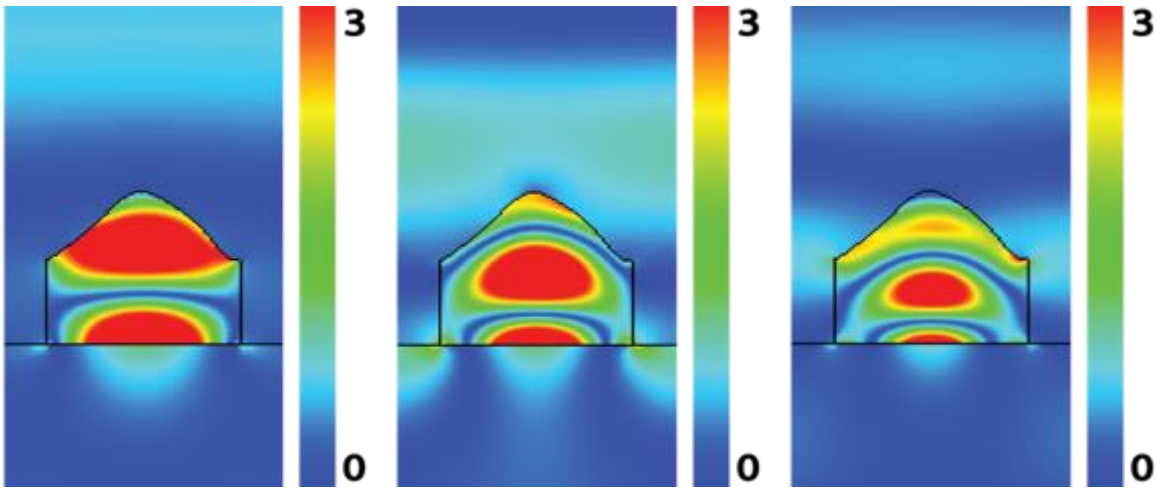

(a)404THz (b)505THz (c)620THz

Figure 5.5 Electric field distribution of model with nine design variables

By designing the artificial structure made of the naturally existing silicon material, a new material with optical properties beyond its constituent material is created. At certain frequencies, the new material can strongly reflect light just like metal, and to some extent, beyond metal. For applications where high power reflection is required, dielectric metamaterial mirrors work much better than metal. Although metal shows high reflection, the reflection cannot reach 100%. When high power light is illuminated on the metal, small portion of the light will be absorbed due to the Ohmic loss of metal. Unlike dielectric materials such as silicon, metal has a lower melting point and is not stable at high temperature. For that reason, absorbing even a tiny portion of the high power laser can lead to severe damage of the metal mirror. On the contrary, the dielectric metamaterial mirror can perfectly reflect light. And due to its high melting temperature, it is more desirable for applications where high power illumination is needed. In addition, through optimization of the metamaterial topology, one can significantly increase the reflection bandwidth. Therefore, the reflected light energy and device efficiency can be greatly enhanced.

Simulation of 3D Metamaterial Model

For verification of 3D solver for metamaterial simulations, we simulated a single-negative all-dielectric metamaterial, comprised of a single layer of cylindrical silicon resonators on a silicon-on-insulator substrate, as shown in Fig.5.6.

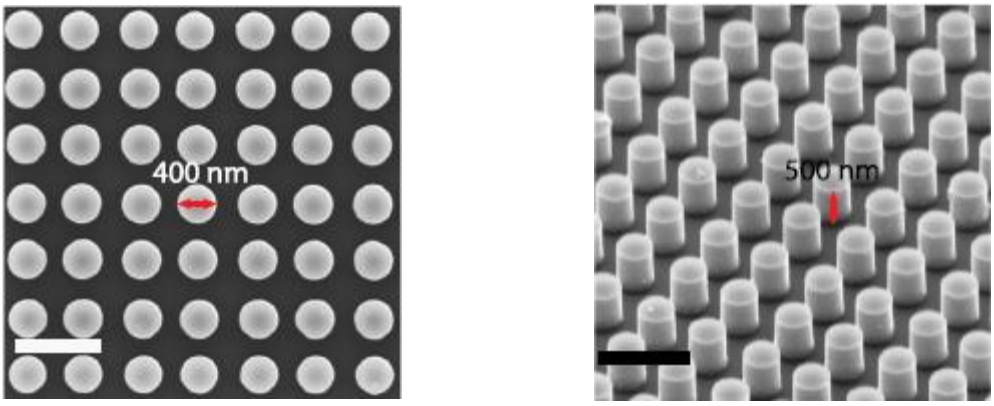

(a) Top view (b) Isometric view

Figure 5.6 SEM images of periodic Si cylinder-based metamaterials[44]

Performance test is run on different meshes for the simulation of the metamaterial perfect reflector, and the results are compared with CST Microwave Studio®. As shown in Fig.5.7, for p1 element, as the mesh becomes finer, the error becomes smaller. Results for p2 elements show good agreement with the results of commercial software even with coarse mesh. The metamaterial perfect reflector possesses peak reflectance over 99% across a 100 nm wide bandwidth in the short-wavelength infrared region. Further optimization can be conducted on this case to obtain desired bandwidth.

The sensitivity analysis technology can be developed to 3D cases for future work. This test case will be a good basic design model for further optimization.

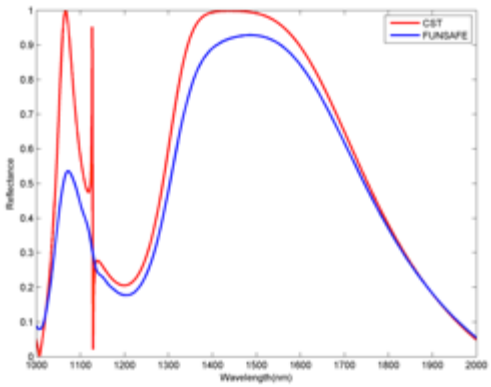

(a) P1 element on Coarse Mesh

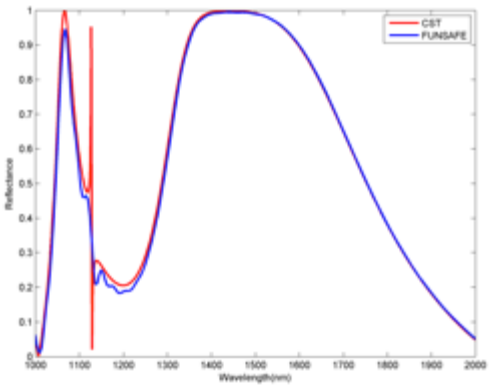

(b) P2 element on Coarse Mesh

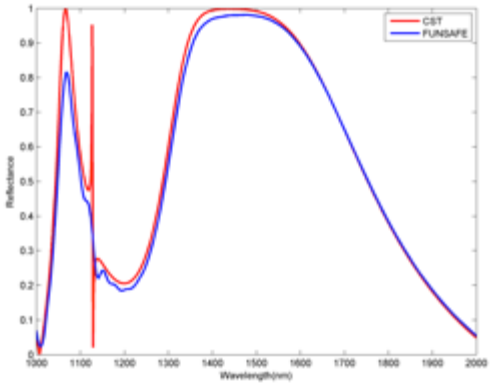

(c) P1 element on Medium Mesh

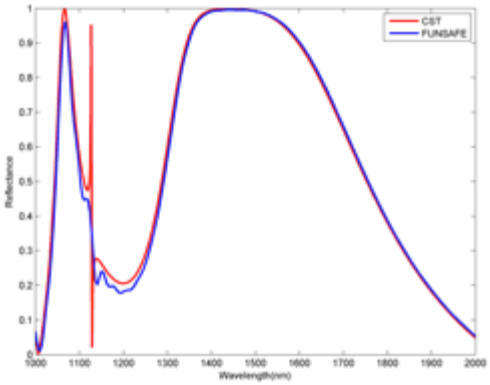

(d) P2 element on Medium Mesh

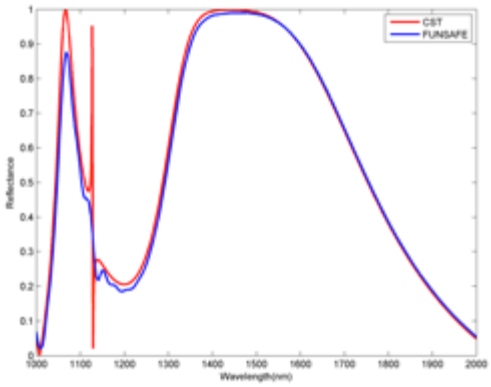

(e) P1 element on Fine Mesh

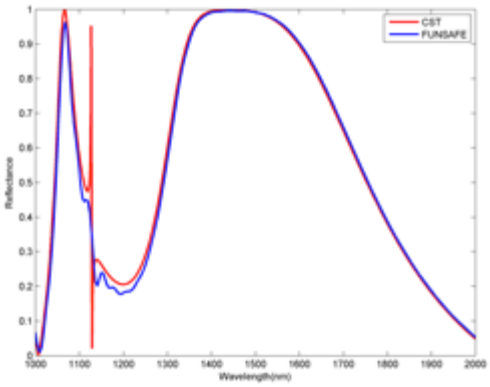

(d) P2 element on Fine Mesh

Figure 5.7 Simulation Results of Reflectance of 3D Metamaterial

CHAPTER VI

CONCLUSION

A Petrov-Galerkin finite element method is applied for the analysis of optical structures: photonic crystals and electromagnetic metamaterials. Implicit time integration is applied in the time domain and quadratic elements are utilized for spatial discretization. A Gaussian pulse is employed as the excitation for the optical structures, which allows the frequency-based characteristics to be obtained in one time-domain calculation. Gradient-based optimization, based on a discrete adjoint formulation for sensitivity analysis, is utilized for optimization of the optical structures.

The first design case is the photonic crystal. The theory and procedures of calculating the photonic band diagram are discussed. Band diagrams of photonic crystals in both square lattice and triangular lattice are calculated and compared with well-recognized band gap calculation software MPB[78] for verification. The sensitivities obtained using the discrete adjoint formulation are compared with results from the finite difference method and forward sensitivity method for verification. Optimization of photonic band gaps is realized by a combination of the electromagnetics simulation code, the time accurate adjoint-based method for sensitivity analysis, the linear elasticity solver for mesh smoothing and an optimization package. The application of photonic crystals as optical waveguide is discussed. The optimized photonic crystals can be used as multi-band optical waveguides for applications in telecommunication.

The second design case is the all-dielectric metamaterial. By designing the

artificial structure, made from existing silicon material, a new effective material with optical properties beyond its constituent material is created. At certain frequencies, the new material can strongly reflect light similar to metal, and to some extent, beyond metallic materials. The simulation results for the base design case are compared with results of HFSS for verification. Utilizing the current shape optimization procedure, the FWHM of reflection was increased from 111THz to 303THz. The optimized broadband metamaterial can be used as dielectric metamaterial mirrors for applications where high power reflection is required.

For verification of the 3D solver for metamaterial simulations, a 3D metamaterial was simulated. The simulation results are compared with CST Microwave Studio® for verification. The grid convergence behavior is demonstrated on meshes with different sizes, which are applied with both p1 and p2 element types.

In future work, the sensitivity analysis technology should be extended to 3D cases for more realistic structures and practical optimization. Moreover, dispersive materials should be introduced for optimization of metamaterials made of metallic materials. Finally, nonlinear materials, whose permittivity and permeability depend on the strength of the fields, should be developed to extend the application domain of the current optimization procedure.

REFERENCES

[1] J. D. Joannopoulos, P. R. Villeneuve, and S. Fan, "Photonic crystals: putting a new twist on light," *Nature,* vol. 386, pp. 143-149, 1997.

[2] J. D. Joannopoulos, S. G. Johnson, J. N. Winn, and R. D. Meade, *Photonic crystals: molding the flow of light*: Princeton university press, 2011.

[3] J. B. Pendry, A. J. Holden, D. Robbins, and W. Stewart, "Magnetism from conductors and enhanced nonlinear phenomena," *IEEE transactions on microwave theory and techniques,* vol. 47, pp. 2075-2084, 1999.

[4] D. R. Smith, W. J. Padilla, D. Vier, S. C. Nemat-Nasser, and S. Schultz, "Composite medium with simultaneously negative permeability and permittivity," *Physical review letters,* vol. 84, p. 4184, 2000.

[5] R. Liu, Q. Cheng, T. Hand, J. J. Mock, T. J. Cui, S. A. Cummer, *et al.*, "Experimental demonstration of electromagnetic tunneling through an epsilon-near-zero metamaterial at microwave frequencies," *Physical review letters,* vol. 100, p. 023903, 2008.

[6] N. Engheta, A. Salandrino, and A. Alù, "Circuit elements at optical frequencies: nanoinductors, nanocapacitors, and nanoresistors," *Physical Review Letters,* vol. 95, p. 095504, 2005.

[7] J. Pendry, "A chiral route to negative refraction," *Science,* vol. 306, pp. 1353-1355, 2004.

[8] S. Zhang, Y.-S. Park, J. Li, X. Lu, W. Zhang, and X. Zhang, "Negative refractive index in chiral metamaterials," *Physical review letters,* vol. 102, p. 023901, 2009.

[9] N. Landy, S. Sajuyigbe, J. Mock, D. Smith, and W. Padilla, "Perfect metamaterial absorber," *Physical review letters,* vol. 100, p. 207402, 2008.

[10] O. F. Siddiqui, M. Mojahedi, and G. V. Eleftheriades, "Periodically loaded transmission line with effective negative refractive index and negative group velocity," *IEEE Transactions on Antennas and Propagation,* vol. 51, pp. 2619-2625, 2003.

[11] G. Dolling, C. Enkrich, M. Wegener, C. M. Soukoulis, and S. Linden, "Simultaneous negative phase and group velocity of light in a metamaterial," *Science,* vol. 312, pp. 892-894, 2006.

[12] D. Schurig, J. Mock, B. Justice, S. A. Cummer, J. B. Pendry, A. Starr, *et al.*, "Metamaterial electromagnetic cloak at microwave frequencies," *Science,* vol. 314, pp. 977-980, 2006.

[13] J. Yao, Z. Liu, Y. Liu, Y. Wang, C. Sun, G. Bartal, *et al.*, "Optical negative refraction in bulk metamaterials of nanowires," *Science,* vol. 321, pp. 930-930, 2008.

[14] J. B. Pendry, D. Schurig, and D. R. Smith, "Controlling electromagnetic fields," *science,* vol. 312, pp. 1780-1782, 2006.

[15] J. Valentine, J. Li, T. Zentgraf, G. Bartal, and X. Zhang, "An optical cloak made of dielectrics," *Nature materials,* vol. 8, pp. 568-571, 2009.
[16] N. Kundtz, D. A. Roberts, J. Allen, S. Cummer, and D. R. Smith, "Optical source transformations," *Optics express,* vol. 16, pp. 21215-21222, 2008.
[17] D. A. Genov, S. Zhang, and X. Zhang, "Mimicking celestial mechanics in metamaterials," *Nature Physics,* vol. 5, pp. 687-692, 2009.
[18] E. E. Narimanov and A. V. Kildishev, "Optical black hole: Broadband omnidirectional light absorber," *Applied Physics Letters,* vol. 95, p. 041106, 2009.
[19] N. Kundtz and D. R. Smith, "Extreme-angle broadband metamaterial lens," *Nature materials,* vol. 9, pp. 129-132, 2010.
[20] T. Zentgraf, J. Valentine, N. Tapia, J. Li, and X. Zhang, "An optical "Janus" device for integrated photonics," *Advanced Materials,* vol. 22, pp. 2561-2564, 2010.
[21] Z. J. Coppens, W. Li, D. G. Walker, and J. G. Valentine, "Probing and controlling photothermal heat generation in plasmonic nanostructures," *Nano letters,* vol. 13, pp. 1023-1028, 2013.
[22] W. Li, Z. J. Coppens, D. G. Walker, and J. G. Valentine, "Electron beam physical vapor deposition of thin ruby films for remote temperature sensing," *Journal of Applied Physics,* vol. 113, p. 163509, 2013.
[23] W. Li, "Photothermal and Photoelectrical Energy Conversion in Plasmonic Nanostructures," 2016.
[24] W. Li, Z. J. Coppens, L. V. Besteiro, W. Wang, A. O. Govorov, and J. Valentine, "Circularly polarized light detection with hot electrons in chiral plasmonic metamaterials," *Nature communications,* vol. 6, 2015.
[25] W. Li and J. Valentine, "Metamaterial perfect absorber based hot electron photodetection," *Nano letters,* vol. 14, pp. 3510-3514, 2014.
[26] W. Li and J. G. Valentine, "Harvesting the loss: surface plasmon-based hot electron photodetection," *Nanophotonics,* vol. 6, pp. 177-191, 2017.
[27] W. Li, Y. Shi, K. Chen, L. Zhu and S. Fan, "A Comprehensive Photonic Approach for Solar Cell Cooling," *ACS Photonics,* 2017, DOI: 10.1021/acsphotonics.7b00089.
[28] A. Boltasseva and H. A. Atwater, "Low-loss plasmonic metamaterials," *Science,* vol. 331, pp. 290-291, 2011.
[29] N. I. Zheludev, "The road ahead for metamaterials," *Science,* vol. 328, pp. 582-583, 2010.
[30] C. M. Soukoulis and M. Wegener, "Past achievements and future challenges in the development of three-dimensional photonic metamaterials," *Nature Photonics,* vol. 5, pp. 523-530, 2011.
[31] J. Zhou, T. Koschny, M. Kafesaki, E. Economou, J. Pendry, and C. Soukoulis, "Saturation of the magnetic response of split-ring resonators at optical frequencies," *Physical review letters,* vol. 95, p. 223902, 2005.
[32] Q. Zhao, L. Kang, B. Du, H. Zhao, Q. Xie, X. Huang, *et al.*, "Experimental demonstration of isotropic negative permeability in a three-dimensional dielectric composite," *Physical review letters,* vol. 101, p. 027402, 2008.
[33] F. Zhang, Q. Zhao, L. Kang, J. Zhou, and D. Lippens, "Experimental verification of isotropic and polarization properties of high permittivity-based metamaterial," *Physical Review B,* vol. 80, p. 195119, 2009.

[34] B.-I. Popa and S. A. Cummer, "Compact dielectric particles as a building block for low-loss magnetic metamaterials," *Physical review letters,* vol. 100, p. 207401, 2008.
[35] J. A. Schuller, R. Zia, T. Taubner, and M. L. Brongersma, "Dielectric metamaterials based on electric and magnetic resonances of silicon carbide particles," *Physical review letters,* vol. 99, p. 107401, 2007.
[36] J. C. Ginn, I. Brener, D. W. Peters, J. R. Wendt, J. O. Stevens, P. F. Hines, *et al.*, "Realizing optical magnetism from dielectric metamaterials," *Physical review letters,* vol. 108, p. 097402, 2012.
[37] L. Peng, L. Ran, H. Chen, H. Zhang, J. A. Kong, and T. M. Grzegorczyk, "Experimental observation of left-handed behavior in an array of standard dielectric resonators," *Physical review letters,* vol. 98, p. 157403, 2007.
[38] X. Cai, R. Zhu, and G. Hu, "Experimental study for metamaterials based on dielectric resonators and wire frame," *Metamaterials,* vol. 2, pp. 220-226, 2008.
[39] Y. Yang, W. Wang, P. Moitra, I. I. Kravchenko, D. P. Briggs, and J. Valentine, "Dielectric meta-reflectarray for broadband linear polarization conversion and optical vortex generation," *Nano letters,* vol. 14, pp. 1394-1399, 2014.
[40] K. Vynck, D. Felbacq, E. Centeno, A. Căbuz, D. Cassagne, and B. Guizal, "All-dielectric rod-type metamaterials at optical frequencies," *Physical review letters,* vol. 102, p. 133901, 2009.
[41] J. r. Sautter, I. Staude, M. Decker, E. Rusak, D. N. Neshev, I. Brener, *et al.*, "Active tuning of all-dielectric metasurfaces," *ACS nano,* vol. 9, pp. 4308-4315, 2015.
[42] S. Liu, M. B. Sinclair, T. S. Mahony, Y. C. Jun, S. Campione, J. Ginn, *et al.*, "Optical magnetic mirrors without metals," *Optica,* vol. 1, pp. 250-256, 2014.
[43] M. Esfandyarpour, E. C. Garnett, Y. Cui, M. D. McGehee, and M. L. Brongersma, "Metamaterial mirrors in optoelectronic devices," *Nature nanotechnology,* vol. 9, pp. 542-547, 2014.
[44] P. Moitra, B. A. Slovick, W. Li, I. I. Kravchencko, D. P. Briggs, S. Krishnamurthy, *et al.*, "Large-scale all-dielectric metamaterial perfect reflectors," *ACS Photonics*, vol. 2, pp. 692-698, 2015.
[45] P. Moitra, B. A. Slovick, Z. G. Yu, S. Krishnamurthy, and J. Valentine, "Experimental demonstration of a broadband all-dielectric metamaterial perfect reflector," *Applied Physics Letters,* vol. 104, p. 171102, 2014.
[46] K. Yee, "Numerical solution of initial boundary value problems involving Maxwell's equations in isotropic media," *Antennas and Propagation, IEEE Transactions on,* vol. 14, pp. 302-307, 1966.
[47] C. o. AMERICA, "CST STUDIO SUITE 2011: INTEGFRATING SIMULATION TECHNOLOGY," *Microwave Journal,* vol. 53, pp. 92-96, Dec 2010.
[48] V. Shankar, W. Hall, and A. H. Mohammadian, "A CFD-based finite-volume procedure for computational electromagnetics-interdisciplinary applications of CFD methods," in *9th AIAA Computational Fluid Dynamics Conference*, 1989, pp. 551-564.
[49] J. S. Shang and D. Gaitonde, "Characteristic-based, time-dependent Maxwell equation solvers on a general curvilinear frame," *AIAA journal,* vol. 33, pp. 491-498, 1995.

[50] J.-M. Jin, *The finite element method in electromagnetics*. New York: Wiley, 1993.
[51] ANSOFT, "HFSS(TM) 12.0: HIGH PERFORMANCE COMPUTING," *Microwave Journal*, vol. 52, pp. 118-120, Nov 2009.
[52] A. N. Brooks and T. J. Hughes, "Streamline upwind/Petrov-Galerkin formulations for convection dominated flows with particular emphasis on the incompressible Navier-Stokes equations," *Computer methods in applied mechanics and engineering*, vol. 32, pp. 199-259, 1982.
[53] W. K. Anderson, L. Wang, S. Kapadia, C. Tanis, and B. Hilbert, "Petrov–Galerkin and discontinuous-Galerkin methods for time-domain and frequency-domain electromagnetic simulations," *Journal of Computational Physics*, vol. 230, pp. 8360-8385, 2011.
[54] X. Zhang, "Higher-order Petrov-Galerkin methods for analysis of antennas," 2013.
[55] D. J. Mavriplis, "Discrete adjoint-based approach for optimization problems on three-dimensional unstructured meshes," *AIAA journal*, vol. 45, pp. 741-750, 2007.
[56] W. K. Anderson and V. Venkatakrishnan, "Aerodynamic design optimization on unstructured grids with a continuous adjoint formulation," *Computers & Fluids*, vol. 28, pp. 443-480, 1999.
[57] E. J. Nielsen and W. K. Anderson, "Recent improvements in aerodynamic design optimization on unstructured meshes," *AIAA journal*, vol. 40, pp. 1155-1163, 2002.
[58] J. Elliott and J. Peraire, "Practical three-dimensional aerodynamic design and optimization using unstructured meshes," *AIAA journal*, vol. 35, pp. 1479-1485, 1997.
[59] L. Wang, D. J. Mavriplis, and K. Anderson, "Unsteady discrete adjoint formulation for high-order discontinuous Galerkin discretizations in time-dependent flow problems," in *48th AIAA Aerospace Sciences Meeting Including the New Horizons Forum and Aerospace Exposition, Orlando, Florida*, 2010.
[60] W. Lin, W. K. Anderson, J. C. Newman III, and X. Zhang, "Shape Optimization of Two-Dimensional Acoustic Metamaterials and Phononic Crystals with a Time-Dependent Adjoint Formulation," *AIAA SciTech*, pp. 2016-1908, 2016.
[61] W. Lin, J. C. Newman III, and W. K. Anderson, "Broadband Shape and Topology Optimization of Acoustic Metamaterials and Phononic Crystals," in *17th AIAA/ISSMO Multidisciplinary Analysis and Optimization Conference, AIAA Aviation and Aeronautics Forum and Exposition 2016*, 2016.
[62] W. Lin, J. C. Newman III, W. K. Anderson, and X. Zhang, "Shape Optimization of Acoustic Metamaterials and Phononic Crystals with a Time-Dependent Adjoint Formulation: Extension to Three-Dimensions," in *17th AIAA/ISSMO Multidisciplinary Analysis and Optimization Conference, AIAA Aviation and Aeronautics Forum and Exposition 2016*, 2016.
[63] W. Lin, "Design optimization of acoustic metamaterials and phononic crystals with a time domain method," 2016.
[64] X. Zhang, J. C. Newman III, W. Lin, and W. K. Anderson, "Time-Dependent Adjoint Formulation for Metamaterial Optimization using Petrov-Galerkin Methods."

[65] T. J. Barth, "Numerical methods for gasdynamic systems on unstructured meshes," in *An introduction to recent developments in theory and numerics for conservation laws*, ed: Springer, 1999, pp. 195-285.
[66] B. Cockburn, S. Hou, and C.-W. Shu, "The Runge-Kutta local projection discontinuous Galerkin finite element method for conservation laws. IV. The multidimensional case," *Mathematics of Computation*, vol. 54, pp. 545-581, 1990.
[67] F. Assous and E. Sonnendrücker, "Joly–Mercier boundary condition for the finite element solution of 3D Maxwell equations," *Mathematical and Computer Modelling*, vol. 51, pp. 935-943, 2010.
[68] P. L. Roe, "Approximate Riemann solvers, parameter vectors, and difference schemes," *Journal of computational physics*, vol. 43, pp. 357-372, 1981.
[69] B. M. Adams, W. Bohnhoff, K. Dalbey, J. Eddy, M. Eldred, D. Gay, *et al.*, "DAKOTA, A Multilevel Parallel Object-Oriented Framework for Design Optimization, Parameter Estimation, Uncertainty Quantification, and Sensitivity Analysis: Version 5.0 User's Manual," *Sandia National Laboratories, Tech. Rep. SAND2010-2183*, 2009.
[70] J. Meza, R. Oliva, P. Hough, and P. Williams, "OPT++: An object-oriented toolkit for nonlinear optimization," *ACM Transactions on Mathematical Software (TOMS)*, vol. 33, p. 12, 2007.
[71] D. U. Manual, "Version 4.20," *Vanderplaats Research and Development*, 1995.
[72] J. C. Meza, "OPT++: An object-oriented class library for nonlinear optimization," Tech. Rep. SAND94-8225, Sandia National Laboratories1994.
[73] J. J. Moré and D. J. Thuente, "Line search algorithms with guaranteed sufficient decrease," *ACM Transactions on Mathematical Software (TOMS)*, vol. 20, pp. 286-307, 1994.
[74] S. L. Karman, "Unstructured viscous layer insertion using linear-elastic smoothing," *AIAA journal*, vol. 45, pp. 168-180, 2007.
[75] C. Kittel, *Introduction to solid state*: John Wiley & Sons, 1966.
[76] Y. Hao and R. Mittra, *FDTD modeling of metamaterials: Theory and applications*: Artech house, 2008.
[77] S. Rajamohan, "A Streamline Upwind/Petrov-Galerkin FEM based time-accurate solution of 3D time-domain Maxwell's equations for dispersive materials," 2014.
[78] S. G. Johnson and J. Joannopoulos, "The MIT photonic-bands package," *from Internet Homepage* http://abinitio. *mit. edu/mpb*, 2008.

VITA

Xueying Zhang was born in Harbin, Heilongjiang, China. She graduated from Harbin No.3 High School in 2007. She earned her Bachelor's degree in Electrical Engineering from Harbin Institute of Technology in July, 2011. After graduation, Xueying accepted a Graduate Research Assistantship from the SimCenter at the University of Tennessee at Chattanooga. She worked with Dr. Kyle Anderson and earned her Master's degree in Computational Engineering in December, 2013. She continued and graduated with a Ph.D in Computational Engineering under the supervision of Dr. James Newman and Dr. Kyle Anderson in May, 2017.